Numerical Investigation of River Discharge and Tidal Variation Impact on Salinity Intrusion in a Generic River Delta Through Idealized Modelling

Constantinos Matsoukis[1,3] · Laurent O. Amoudry[2] · Lucy Bricheno[2] · Nicoletta Leonardi[1]

Abstract

Salinity in deltaic systems is expected to increase in the near future due to sea level rise. This will cause severe environmental consequences because salinity can be detrimental to agriculture, aquaculture and human consumption. Tidal dynamics are important in regulating salinity in river deltas. However, there is still uncertainty about the influence of different tidal amplitudes on deltas' salinity. This paper investigates the impact of various tidal amplitudes on the spatiotemporal salinity distribution in deltas through three-dimensional idealized modelling. Numerical simulations are carried out with a common hydrograph and different tidal ranges. Both tide-influenced and river-dominated cases were considered. Results suggest that small increases in the tidal amplitude in river-dominated or low tidal regimes cases can have positive effects against salinization. Tide-induced mixing helps to increase freshwater areas and volumes. The water in the delta remains fresh for longer periods in scenarios representative of microtidal regimes. Further increases in the tidal amplitude to meso- and macrotidal levels reverse these effects and reduce freshwater areas and volumes. Results were used to test how salinity correlates with channel orders and river discharge in the presence of tides. These correlations are controlled more by bathymetry than tidal forcing. This study provides important insights into how changes in tidal range could impact spatiotemporal salinity distributions in deltas.

Keywords Salinity · River deltas · Tidal amplitude · River discharge · Idealized modelling

Introduction

River deltas are coastal ecosystems with highly fertile soils and productive waters and are attractive places for living and working with dense populations and high economic activity (Ericson et al. 2006; Fagherazzi et al. 2015; Bianchi 2016; Nicholls et al. 2018). Climate change challenges the sustainability and maintenance of deltaic systems worldwide.

✉ Constantinos Matsoukis
  c.matsoukis@liverpool.ac.uk;
  constantinos.matsoukis@stir.ac.uk

1 Department of Geography and Planning, School of Environmental Sciences, University of Liverpool, Roxby Building, Chatham St, Liverpool L69 7ZT, UK

2 National Oceanography Centre, Joseph Proudman Building, 6 Brownlow Street, Liverpool, Merseyside L3 5DA, UK

3 Department of Biological and Environmental Sciences, Faculty of Natural Sciences, University of Stirling, Cottrell Building, Stirling FK9 4 LA, UK

Sea level rise (SLR) increases the salinity in deltaic regions and causes an upstream intrusion of the tidal saltwater zone (Gornitz 1991; Bhuiyan and Dutta 2012; Hong and Shen 2012; Hong et al. 2020; Bricheno et al. 2021). Saltwater intrusion (SWI) is an important phenomenon in coastal zones that is driven by both anthropogenic (e.g. groundwater extraction) and natural (e.g. tidal inundation) factors (White and Kaplan, 2017; Rahman et al., 2019) and causes serious problems in households, agriculture, irrigation and industry (Allison 1964; Smedema and Shiati 2002; Zhang et al. 2011). Salinization contaminates rivers, aquifers and soils decreasing freshwater storage and water quality (Gornitz 1991). High salinity reduces soil fertility resulting in low crop yield (Bhuiyan and Dutta 2012). For example, severe reduction in rice and wheat production is reported in the Bangladesh delta where many freshwater rice paddies have been converted to brackish water shrimp farms (Sarwar 2005; Bricheno and Wolf 2018). Conversion of freshwater to brackish or saltwater habitats has also occurred in the Mississippi Delta where serious ecological degradation is taking place because of

flooding (Holm and Sasser 2001; Kaplan et al. 2010). SWI is hazardous for many marine and vegetation species that have limited tolerance to salinity. For instance, some types of phytoplankton, larvae fish and shrimps usually survive only in environments with less than 2 g/kg salinity (Jassby et al. 1995; Hutton et al. 2016). Other vegetation species in the Louisiana wetlands and Mississippi Delta (Sagittaria Latifolia, Sagittaria Lancifolia, phragmites australis) also require less than 2 g/kg salinity (Visser et al. 2012; White et al. 2019). In addition, high salinity may be responsible for plant stress and mortality and hampering tree production (Kaplan et al. 2010; Bhuiyan and Dutta 2012). Moreover, human health can be affected by salinization through water consumption. Drinking water should not contain more than 1 g/kg salinity (de Vos 1990; Dasgupta et al. 2015; Sherin et al. 2020). Saline water environment is favourable for the development of microbes related to water borne diseases such as cholera or diarrhoea. Many cholera outbreaks in Bangladesh occurred after flooding because the water supply was contaminated (Sarwar 2005). Saline water has been also reported as a leading cause for hypertension (Rahman et al. 2019). SWI causes currently similar problems to many deltas worldwide, e.g. Mekong (Eslami et al. 2019), Yangtze (Chen et al. 2001; Dai et al. 2011; Qiu and Zhu 2015), Pearl River (Liu et al. 2019; Hong et al. 2020), Nile (Frihy 2003), Mississippi (Day et al. 2005) and Bangladesh (Rahman 2015; Yang et al. 2015; Bricheno et al. 2016, 2021; Sherin et al. 2020).

Salt intrusion in estuaries is mainly determined by river discharge, estuary shape, tidal and wave forcing (Nguyen et al. 2008; Dai et al. 2011; Gong and Shen 2011; Maccready et al. 2018). Although the role of river discharge on the salinity is usually dominant, this is low compared to the tidal flow during low flow periods when salt intrusion matters the most (Nguyen et al. 2008; Zhang et al. 2010). For example, the Yangtze delta experiences saltwater intrusion during low flows and under strong tidal conditions affecting domestic water usage for millions of people in the city of Shanghai (Qiu and Zhu 2015). The interaction of freshwater flow and tide establishes an estuarine circulation (or exchange flow) with seaward flow near the surface and landward flow near the bottom layer (Pritchard 1956; Hansen and Rattray 1965; Dyer 1973; MacCready and Geyer 2010) although other circulation modes are possible too depending on the level of river and tidal forcing and variations in mixing (Geyer and MacCready 2014). Landward salt transport is driven either by exchange flow or tidal dispersion (Banas et al. 2004; Lerczak et al. 2006; MacCready 2007; MacCready and Geyer 2010). Tidal processes determine the large-scale salt transport and distribution by influencing stratification and exchange flow (Liu et al. 2007; MacCready and Geyer 2010). The exchange flow can be increased by tidal asymmetry especially during flood tides while strain-induced stratification might develop

at the ebb tide (Simpson et al. 1990; Jay and Musiak 1994; MacCready and Geyer 2010).

Climate change effects on the annual water cycle are expected to cause fluctuations in the river discharge that together with SLR will impact tidal dynamics as well (Bricheno et al. 2021). SLR may cause alterations to tidal range and currents on local, regional and global scale (Zhong et al. 2008; Hong and Shen 2012; Haigh et al. 2020; Hong et al. 2020). These will be more acute over large shallow coastal waters such as deltas while the tides remain unaffected in deeper waters (Nguyen 2016). Nguyen (2016) identifies the following mechanisms as responsible for these changes in tidal regimes: (1) increase in the tidal wave phase speed, (2) direction change, (3) tidal friction decrease and (4) frequent flooding of inter-tidal areas. Very flat deltas such as the Mekong will be highly affected. Increases of the tidal range due to SLR have been reported in the Chesapeake Bay (Zhong et al. 2008), Yangtze Delta (Qiu and Zhu 2015), Bangladesh delta (Bricheno et al. 2021), Mekong delta (Nguyen 2016), Pearl River Delta (Zhang et al 2010) and the Eastern Scheldt estuary (Jiang et al. 2020). Hong and Shen (2012) and Chua and Xu (2014) reported an increase of the estuarine circulation in the Chesapeake and San Francisco Bay respectively due to SLR with a consequent increased upstream salt intrusion.

However, tidal amplitude (TA) can both decrease and increase in response to SLR (Green 2010; Holleman and Stacey 2014; Carless et al. 2016; Pickering et al. 2017) and changes of TA may be proportional (Idier et al. 2017) or not to mean SLR (Pelling et al. 2013). In an idealized study, Du et al. (2018) demonstrated that the tidal range is likely to decrease with SLR in short estuaries with a narrow channel and low-lying shallow areas. This means that deltaic systems may face changes in their tidal forcing with either increases or decreases. Changes in tidal mixing and currents are expected to have implications in saltwater intrusion (Jiang et al. 2020) and thus a delta's salinity distribution. Because the level of these changes can vary a lot globally, there is a need to assess their impact on a system's salinity in a generic and not site-specific manner. This is required in order to take measures and prevent the damage on the human population dependent on deltas and the execution of their activities. There is already enough knowledge on the variation of temporal and spatial salinity distribution in estuaries under the combined forcing of river discharge and tide (Jay 1991; Turrell et al. 1996; Uncles and Stephens 1996; Monismith et al. 2002; Bowen and Geyer 2003; Chen 2004; Prandle 2004; Lerczak et al. 2006; Liu et al. 2007; Ralston et al. 2010; Wei et al. 2016), but there is still a gap concerning channelized networks.

This paper presents a modelling study that predicts the changes that different tidal ranges can cause on the spatiotemporal salinity distribution of a static deltaic system where no morphological changes occur. For this purpose, a

3D numerical model is built in Delft3D for an idealized delta configuration. We follow a minimalist idealization concept (Weisberg 2007), and therefore only retain the core causal factors (influence of river discharge and tides here) controlling a phenomenon (salinity distribution and salt intrusion here). Such an approach relying on idealized or 'exploratory' models (Murray 2002), in which some processes are intentionally omitted and others are simplified, can offer simpler and better explanations of certain behaviours in systems involving many interacting processes (Murray 2002).

A series of simulations is carried out for both river-dominated and tidally influenced deltas. The model is forced in each case with an upstream freshwater flow varying on a daily basis for a period of 1 year and a constant offshore tidal boundary condition. For simplicity low-frequency tidal motions (spring–neap cycle) are omitted and only one semi-diurnal tide is considered in each case. This allows for a direct correspondence between daily discharge values and salinity (when averaged over two tidal cycles) and makes it easier to detect the impact of absolute tidal level on seasonal salinity patterns. Estuarine studies have reported that the tide affects buoyant plumes symmetry (Chao 1990; Isobe 2005; Guo and Valle-Levinson 2007; Lee and Valle-Levinson 2013). To compare the various amplitude effects on plumes' symmetry and structure, the Earth's rotation is neglected to avoid an extra source of asymmetry. In the results analysis, an extra emphasis is given on the changes in freshwater areas, volumes and duration of freshwater conditions since this is what matters probably the most in regard to the activities taking place in a delta.

Matsoukis et al. (2021) related salinity with channel order and river discharge. By classifying the delta channels into stream orders based on the Strahler–Horton method (Horton 1945; Strahler 1952; Smart 1968; Gupta and Mesa 1988; Gleyzer et al. 2004; Reis 2006; Moussa 2009; Chunikhina 2018; Yamamoto 2017), they found that salinity increases with the decrease of the stream order. They also discovered that radial averages of salinity are negatively correlated and exponentially decaying with river discharge through an equation that resembles solutions of the 1D advection–diffusion equation under certain theoretical assumptions. The applicability and robustness of these methods is tested now for a system that includes tidal forcing.

An additional method is implemented next to the Strahler–Horton one that is commonly referred to as width function. This is a method that describes bifurcation in terms of the number of channel links in some distance from the outflow (Kirkby 1976). Width function measures a basin's width distribution in space. Many authors implied a connection between a catchment's width and its hydrologic response (Gupta and Mesa 1988; Rinaldo et al. 1991, 1995; Snell and Sivapalan 1994; Botter and Rinaldo 2003). Collischonn et al. (2017) investigated any impact of the width function to a catchment's hydrograph shape while much earlier, Kirkby (1976) mentioned the network's width influence to peak discharge timings.

The present work aspires to give an insight on the influence of tidal forcing on the salinity inside deltaic systems that could contribute to the efforts for providing solutions against the issue of salinization in deltas.

Methods

An idealized river delta configuration is built using the Delft3D software (Deltares 2013). Delft3D comprises a series of modules to simulate flow, waves, water quality, morphology, sediment transport and ecology. It has been successfully implemented in the past for several applications including the modelling of river deltas, freshwater discharges in bays, stratified density flows and salt intrusion problems (Hu et al. 2009; de Nijs and Pietrzak 2012; Elhakeem and Elshorbagy 2013; Martyr-Koller et al. 2017). More information on Delft3D can be found in its manual (Deltares 2013). The idealized delta derives from a 2D morphological simulation that precedes the simulations with salinity. The setup of the morphological and salinity models is described in the following sections.

Morphological Model Setup

A structured rectangular grid is used that has dimensions 20 km × 22 km and it can be seen in Fig. S1 of the 'Online Resource'. The grid resolution varies from 50 to 200 m in the X direction and between 20 and 100 m in the Y direction of a Cartesian co-ordinate system. An inlet is added starting at the west boundary with 1.3 km length and 380 m width. The resolution is finer close to the inlet and becomes coarser offshore and closer to the boundaries. The grid cell size for building up an idealized delta is subject to certain limitations. Coarse resolution produces channels of constant width usually equal to one or two times the grid space step because adjacent cells transform abruptly from dry to wet. The result would be a network with straight channels and no curvature or meandering. The resolution has to be as finer as possible so that the flow erodes the bed and the suspended sediments are deposited unevenly between adjacent cells forming channels of various widths. For example, previous idealized delta studies done with Delft3D (e.g. Liu et al. 2020; Burpee et al. 2015; Caldwell and Edmonds 2014; Edmonds and Slingerland 2010) all used a 625 m² (25 m × 25 m) grid cell area that is fit for the purpose. However, a very fine resolution requires a relatively small model area regarding computational efficiency. In simulations with salinity, larger model areas are needed to monitor the evolution of the offshore buoyant plume both longitudinally and laterally. With this consideration, the present model's grid cell area within
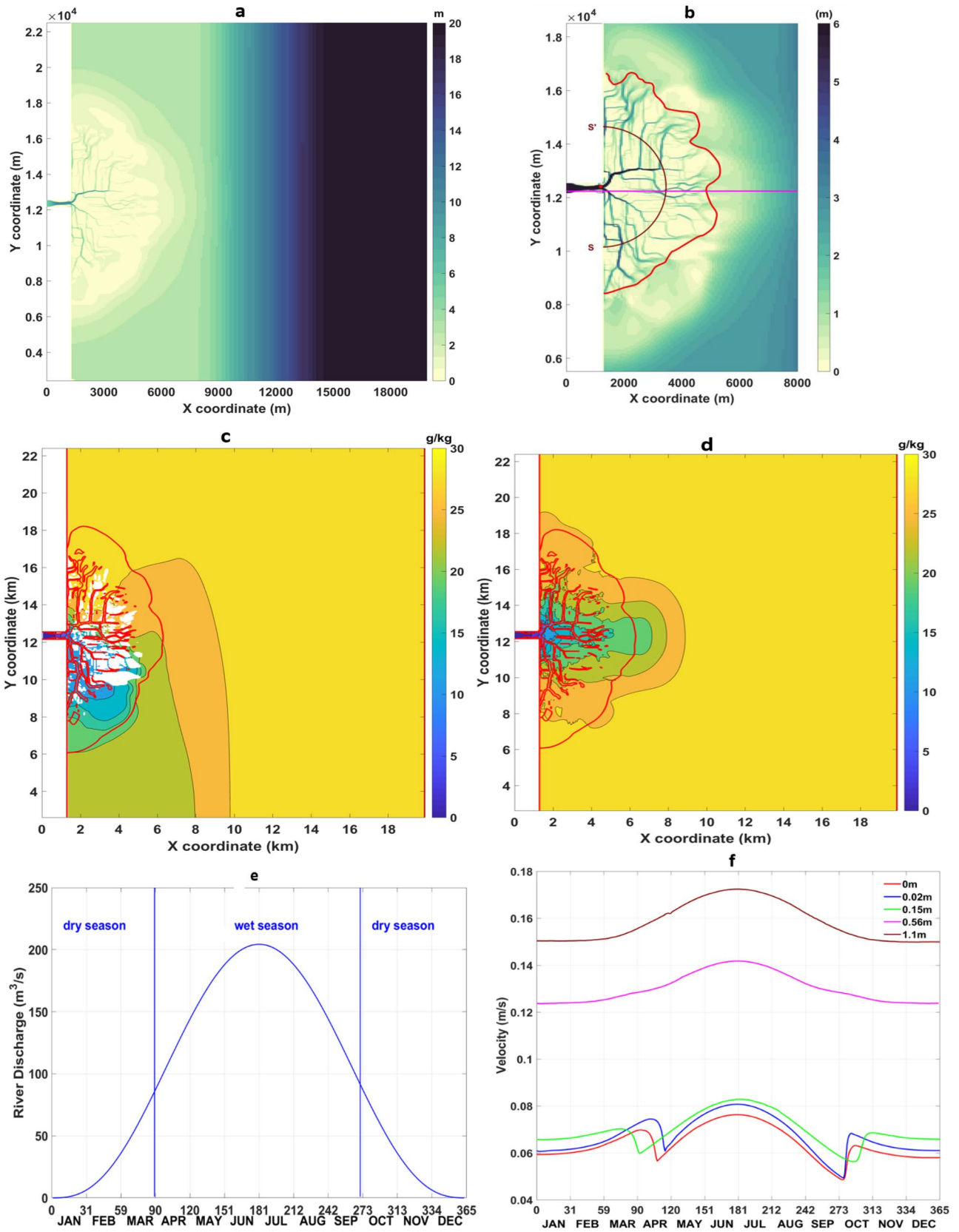
◄Fig. 1 a Model bathymetry. The white-coloured parallelograms left and right of the river inlet indicate inactive cells. The bathymetry starts to deepen incrementally with a 0.5° slope at X = 10 km. **b** Zoom of the bathymetry in the delta area. Notice the much deeper channel on the left of the river inlet (looking seaward). SS' is the semicircle over which salinity is averaged in 'Relation Between Salinity and River Discharge'. The red dot is the centre of the semicircle. The magenta horizontal line is the transect where the vertical salinity distribution is presented in 'Vertical Salinity Distribution in the Tide-Influenced Scenarios'. The red borderline connects the ends of the channels delineating the delta's border. Calculations for Figs. 1f and 6 were done for the area upstream of this border. **c**, **d** Initial conditions for salinity of scenario 1 with zero tidal amplitude and scenario 5 with 1.1-m tidal amplitude respectively. The delta channels and limits are delineated by the red colour line. White areas in panel c indicate dry points above the water level. **e** The idealized hydrograph implemented in the model with the corresponding days and months at the horizontal axis. The vertical lines indicate the limit between dry and wet seasons. **f** The depth-averaged velocity magnitude for the different tidal amplitudes averaged within the delta limits as delineated by the red borderline in panel b

the delta limits was set to 1 km². While a finer grid could have reproduced a more complex channels meandering, the adopted grid has been deemed suitable in consideration of the above and within the context of this manuscript's scope which utilizes stream order considerations. The initial bathymetry is uniform with a depth equal to 3 m up to 10 km from the west (river) boundary. After this point, a bed slope of 0.5° is imposed and the water depth reaches 30 m at the offshore boundary. The model is initiated with no surface elevation throughout the domain and is forced by an upstream steady river discharge equal to 3000 m³/s. The bed subsurface is erodible and has initially a 5-m sediment layer thickness everywhere. The coast on the west boundary is non-erodible and its width is equal to the inlet's length (1.3 km). The grid resolution is such that allows the use of the default Delft3D values for horizontal viscosity/diffusivity equal to 1 m²/s and 10 m²/s respectively. A uniform bottom roughness is considered with a Chezy coefficient equal to 45 m$^{1/2}$/s. A numerical scheme denoted as cyclic method (Stelling and Leendertse 1992) is implemented based on an implicit scheme that does not impose time restrictions. For computational efficiency, the time step is set equal to 12 s. The morphological processes are speeded up by a factor of 175 following the work of Edmonds and Slingerland (2010) and Caldwell and Edmonds (2014).

Zero gradient water level (Neumann condition) is prescribed at the lateral boundaries. A constant surface water elevation is imposed at the offshore boundary. No sediment input is considered at the boundaries. The riverine input carries into the basin equilibrium concentrations of a cohesive and a non-cohesive sediment fraction equal to 0.5 kg/m³ and 0.2 kg/m³ respectively. Values are chosen based on the experiments of Edmonds and Slingerland (2010) in order to obtain a fan-like delta. The 2D model calculates the

suspended sediment transport through the depth-averaged version of the advection–diffusion equation (Caldwell and Edmonds 2014):

$$\frac{\vartheta C}{\vartheta t} + u_x\frac{\vartheta C}{\vartheta x} + u_y\frac{\vartheta C}{\vartheta y} + \frac{\vartheta(u_z - w_s)C}{\vartheta z} = D_x\frac{\vartheta^2 C}{\vartheta x^2} + D_y\frac{\vartheta^2 C}{\vartheta y^2} + D_z\frac{\vartheta^2 C}{\vartheta z^2} \tag{1}$$

C is the concentration of each sediment fraction; u_x, u_y and u_z are the x–y and z directed flow velocities; w_s is the settling velocity; and D_x, D_y and D_z are the directional eddy diffusivities. During the simulation, bed erosion and sedimentation occur throughout the domain under the influence of the river discharge. All the settings (including the discharge) have been selected after a sensitivity analysis where a number of simulations were executed with different values each time until a fan-like delta shape is developed with a typical meandering and channel curvature as the final one presented in Fig. 1a. The morphodynamic model was run for a period of 34 days with the input parameters summarized and listed in the 'Online Resource' (Table S1). The bathymetry exhibits many features common in real deltas such as the delta front slope and the pro delta deepening (Hori et al. 2002; Hori and Saito 2007; Goodbred and Saito 2012), the erosion in front of the delta apex and the downstream shallowing and widening of the channels (Lamb et al. 2012). Special care was taken to allow enough space in the longitudinal and lateral directions for the offshore buoyant plume to develop later in the simulations with salinity.

Salinity Model Setup

The salinity simulations require a 3D model and thus 8 vertical sigma layers are added. The model was tested with finer vertical resolution as well. However, it was found that there is no significant impact on the numerical results by increasing any further the number of layers, most probably due to the shallowness of the delta. Also considering the computational resources for a full year study, this number is deemed sufficient for this specific case.

The delta covers an area of approximately 4.8 km × 8 km as it can be seen in Fig. 1a. Freshwater flow and tidal data are available for most deltas worldwide that could be implemented into the model. However, the size of this idealized delta is much smaller compared to real ones. For example, the Po Delta that is a relatively small one covers an area of 685 km² (Maicu et al. 2018). This is about 18 times the delta area of the present model. Therefore, data manipulation is necessary before introducing them in the model. This is necessary to ensure the model's stability and avoid unrealistic results due to a complete filling of the domain with freshwater in the case of very high discharges or the imposition of extreme saline conditions due to excessive tidal amplitudes for this model's size. Downscaling of magnitudes in

idealized models is not unusual. We consider issues in terms of modelling distortion to be negligible because we are not aiming at reproducing a specific river delta and because the partial differential equations implemented in the model do not differ from those that would be considered for larger or real scales applications. The use of data from real cases only serves the purpose of setting up the model but there is no intention to reproduce the conditions of these real deltas or their configuration and therefore the model results should not be compared with real case studies. In the case of such idealized (or exploratory) models that leave out intentionally certain processes (e.g. waves), the predictions should not involve the magnitudes of the model-dependent variables but the trends in how these variables (e.g. salinity) respond in various conditions (e.g. river or tidal forcing) (Murray 2003).

To create a hydrograph to be introduced in the model, the Po hydrograph of 2009 (Montanari 2012) is scaled down by the ratio of the Po delta over the idealized delta area which is equal to 18 approximately. The hydrograph is converted to a symmetric beta distribution using the following equation (Yue et al. 2002):

$$B(a, b) = \int_0^1 x^{a-1}(1-x)^{b-1}dx$$
$$0 < x < 1; a, b > 0 \tag{2}$$

where x is the variable and a and b are shape parameters. By taking equal shape parameters, a symmetry is obtained with equal flows between the 1st and 2nd semester (day 1 to day 182 and day 183 to day 365 respectively). The idealized hydrograph is presented in Fig. 1e. Many deltas e.g. Yangtze (Lai et al. 2014; Birkinshaw et al. 2017), the Volga (Polonskii and Solodovnikova 2009), Po Delta (Montanari 2012), and the Mississippi (usgs.gov)) present annual flow distributions with a single distinct peak usually in or close to the middle of the year. This shape is very convenient because it allows for an easy distinction between wet and dry seasons so that salinity patterns developed during the relevant periods could be easily detected.

A series of five simulations with the same hydrograph but different tidal amplitudes is carried out: two river-dominated and three tide-influenced cases. The first river-dominated case assumes no tidal water level variation. The four other amplitudes were selected to represent increasing tidal influences. The ratio between freshwater and tidal volume can be expressed by the Canter-Cremers number, also known as the estuary number N, and defined as (Savenije 2005):

$$N = \frac{Q_f T}{P_t} \tag{3}$$

Q_f, T and P_t are the freshwater discharge, the tidal period and prism respectively. High and low estuary numbers indicate larger amount of fresh and saline water respectively entering in the system during a tidal period (Savenije 2005). By implementing Eq. 3, N was calculated using data from four real deltas of which each one corresponds to a nano-,micro-,meso- and macrotidal regime. Equation 3 is worked out to obtain four scaled tidal amplitudes corresponding to each of these tidal regimes by keeping N equal between a real case and the model. To solve Eq. 3 with respect to the model's amplitude, the mean flow of Fig. 1e hydrograph was used.

Density mixing is not expected to be affected (at least significantly) because of the use of scaled flow and amplitudes in the model. To test this, the model was run with the same hydrodynamic forcing but lower salinity and the results did not show any considerable differences. This has been further tested by looking at other non-dimensional parameters such as the Estuarine Richardson number (which considers the tidal velocity in contrast to Canter-Cremers) that was found to decrease with the increase of the amplitude just as the estuary number does (Table 1).

The characteristics of the five simulations are summarized in Table 1. Scenario 2 eventually falls into a river-dominated case because its estuary number is much higher and its amplitude much lower than the three other scenarios. The estuary number of the three tidally influenced cases decreases as the amplitude increases as they were designed to represent micro-, meso- and macrotidal regimes.

The bathymetry is kept constant for the salinity simulations with various amplitudes even though the strength of the tidal forcing can develop morphological features that are not represented in this case. However, we are looking at relatively short time scales that do not exceed 1 year with respect to channels' morphological changes that could take place in decadal scales. This may underestimate the considerable

Table 1 Estuary number, tidal amplitudes and classification for each simulation — in parenthesis the abbreviations for each one of them

Scenario	Estuary number	Scaled model tidal amplitude (m)	Classification
1	n/a	0	River dominated (no tide)
2	0.49	0.02	River dominated (nano tide)
3	0.073	0.15	Micro-tide (micro)
4	0.018	0.56	Meso-tide (meso)
5	0.009	1.1	Macro-tide(macro)

morphodynamic changes that can take place in mesotidal and macrotidal regimes even in relatively short time scales but it is not expected to have a significant impact on our conclusions. Morphological processes are omitted in this work and the model does not include any sediment input because the use of different morphologies would introduce another varying parameter and would severely hinder isolating the effects of tides and rivers.

A spatially constant Chezy coefficient (45 m$^{(1/2)}$/s) is implemented to account for bed roughness. A cyclic implicit numerical scheme is used and the time step is 30 s being the optimum value for both model stability and computational time.

In Delft3D, the horizontal diffusion is resolved by the use of a sub-grid turbulence closure model and a user-defined coefficient used for calibration. The default Delft3D value is implemented (10 m^2/s) securing the model stability. The vertical diffusion is fully modelled by the κ-ε turbulence closure model.

The salt transport is calculated by the 3D advection–diffusion equation for salinity (S):

$$\frac{\partial S}{\partial t} + u\frac{\partial S}{\partial x} + v\frac{\partial S}{\partial y} + w\frac{\partial S}{\partial z} = K_h\frac{\partial^2 S}{\partial x^2} + K_h\frac{\partial^2 S}{\partial y^2} + K_z\frac{\partial^2 S}{\partial z^2} + Ss$$

(4)

K_h and K_z are the horizontal and vertical diffusion coefficients respectively and Ss are source and sink terms.

Boundary Conditions

The tide is prescribed at the offshore boundary in the form of a cosine function with its amplitude defined through the Riemann invariant. In Delft3D, the Riemann invariant is introduced as a user-defined parameter with velocity units (Deltares 2013). An S$_2$ solar tide is introduced and so the tidal period is 12 h in every simulation. Such a simplification is reasonably common in idealized modelling (e.g. Guo and Valle-Levinson 2007) as it significantly simplifies the analysis of the numerical results. Variability due to daily inequalities and at sub-tidal scales (e.g. spring–neap cycles) is neglected with such a tidal forcing but remains beyond the direct scope of the present study. A zero water level gradient (Neumann condition) is implemented at the lateral boundaries. However, the Neumann boundaries in this case are slightly modified to allow the freshwater plume to spread radially with no boundary effects. This can be done by reducing the diffusion coefficient and deactivating the baroclinic pressure terms at the two last grid lines of the lateral boundaries (Deltares 2013). The offshore boundary is considered to be a sea boundary with salinity equal to 30 g/kg. The salinity at the river boundary is set to zero. Free transport is allowed at the lateral boundaries where the model is allowed to calculate its own values. The numerical simulations for salinity do not include any sediment input, the influence of sediments on the baroclinic flow is then neglected and the bathymetry is frozen during the simulation.

Initial Conditions

A spin-up simulation precedes each one of the five scenarios to generate initial conditions for salinity. In these spin-up simulations, the salinity is set equal to 30 g/kg everywhere except for the river boundary where it is zero. The model in this case is forced by the minimum river flow in Fig. 1e, which is equal to the starting value, and the tidal amplitude of each scenario from Table 1. Thus, the experiments begin with different initial conditions, dependent on the tidal range. The simulation is stopped when the ratio of salinity and flow velocity over the last two tidal cycles is equal to 1 and quasi-steady state conditions can be assumed. A time period of 45 days is needed for the simulations to reach a quasi-steady state. The initial conditions for the surface layer of scenarios 1 and 5 are presented in Fig. 1c and d respectively. The salinity distribution in Fig. 1d is symmetric while in Fig. 1c is not. The bathymetry is identified as the main cause of this asymmetry in the no tide case because the branch on the left of the delta apex (facing the sea) is much deeper than the rest of the channels and acts as a flow barrier (Fig. 1b). Its depth reaches almost 9 m when the overall mean channel depth is no more than 3 m. This is further discussed in 'Horizontal Salinity Distribution and Flow Field Evolution with the Tidal Variation'. Earth's rotation may also produce spatial asymmetry and therefore is not included in the simulations to avoid another source of asymmetry.

Results

Horizontal Salinity Distribution and Flow Field Evolution with the Tidal Variation

Map plots in Figs. 2 and 3 provide instantaneous isohalines and flow vectors during dry and wet season for each one of the five simulations 3 h after high water (HW) and low water (LW) respectively at the top layer. Figure 2 displays an instant during ebb and Fig. 3 an instant during flood tide. Considering that the period of the solar tide is 12 h, this means that the tidal level equals the mean water level 3 h after the HW (MTL$_H$) and LW (MTL$_L$). Consequently, the maps display results for times when the flow velocity at the boundary is closer to its maximum value. The maps show results at two instants 6 months apart: 1 day (dry season) and 180 days (wet season) after the start of the simulation. The latter corresponds to the day of the maximum and the former to that of the minimum flow.

Fig. 2 Salinity and flow vectors at the top layer 1 day (dry season, left column) and 180 days (wet season, right column) after the start of the simulation for all amplitudes. The map plots show the salinity and flow conditions 3 h after high water (ebb tide). Salinity increments are at 1 g/kg. Flow vector spacing is 10
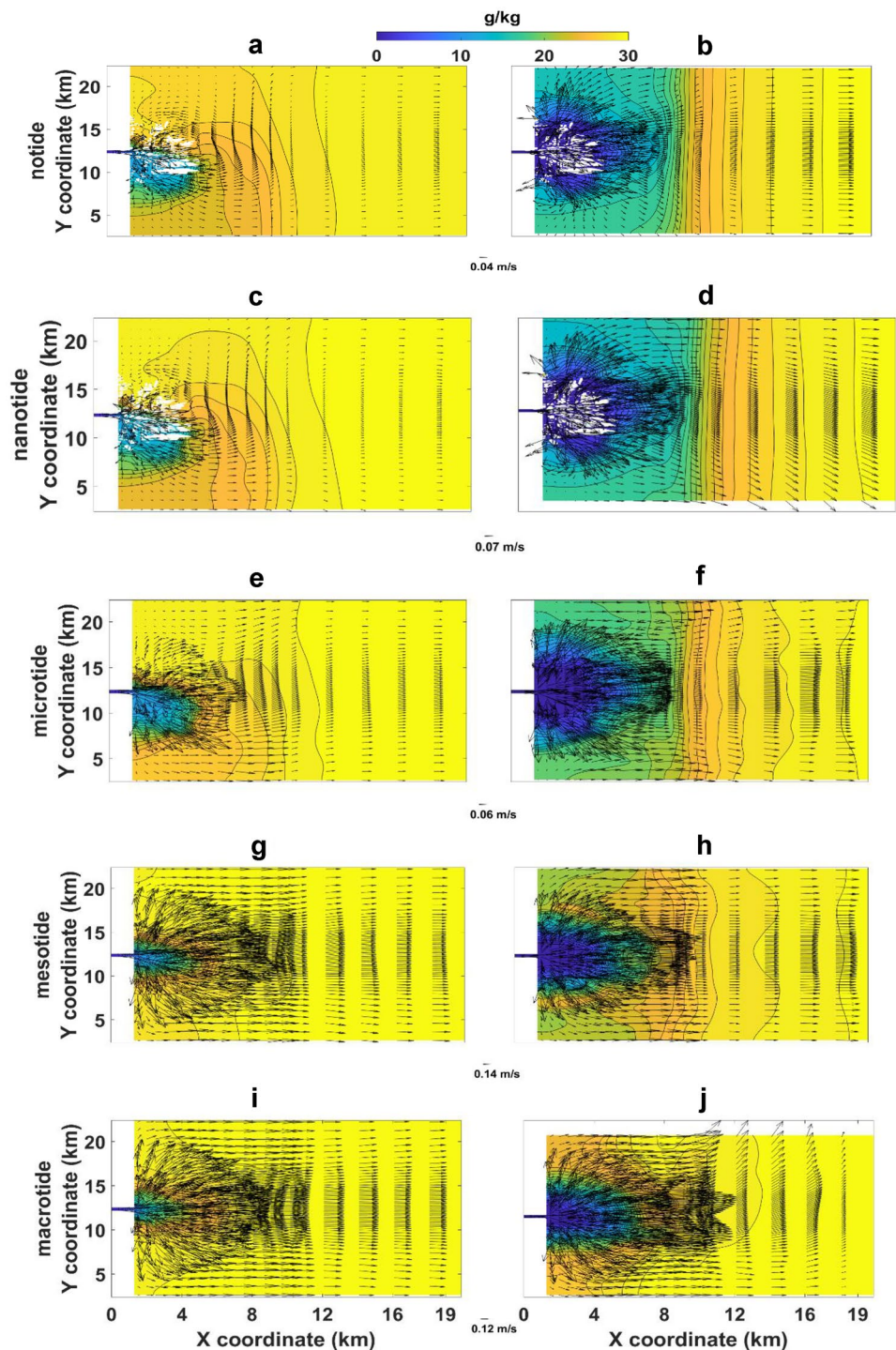
Salinity Variation with Seasonality, Tidal Amplitude and Stage

The spatial salinity distribution at the time of minimum flows is asymmetric for the first two scenarios (river-dominated cases) because it is affected by the bathymetric asymmetry (see 'Initial Conditions'). Higher salinity is present on the left

and lower on the right of the delta apex (looking seaward) as it can be seen in Figs. 2a,c and 3a, c. The channels are shallower on the right side and that allows for a faster decrease of salinity under the freshwater influence while this process is impeded by the much deeper channel on the left side of the inlet. The system moves towards a more symmetrical state when higher flows occur during wet season (Figs. 2b, d

Fig. 3 The same content as in Fig. 2 but 3 h after low water (flood tide). The 0 m amplitude maps are identical but they are included to facilitate the comparison with the other amplitudes
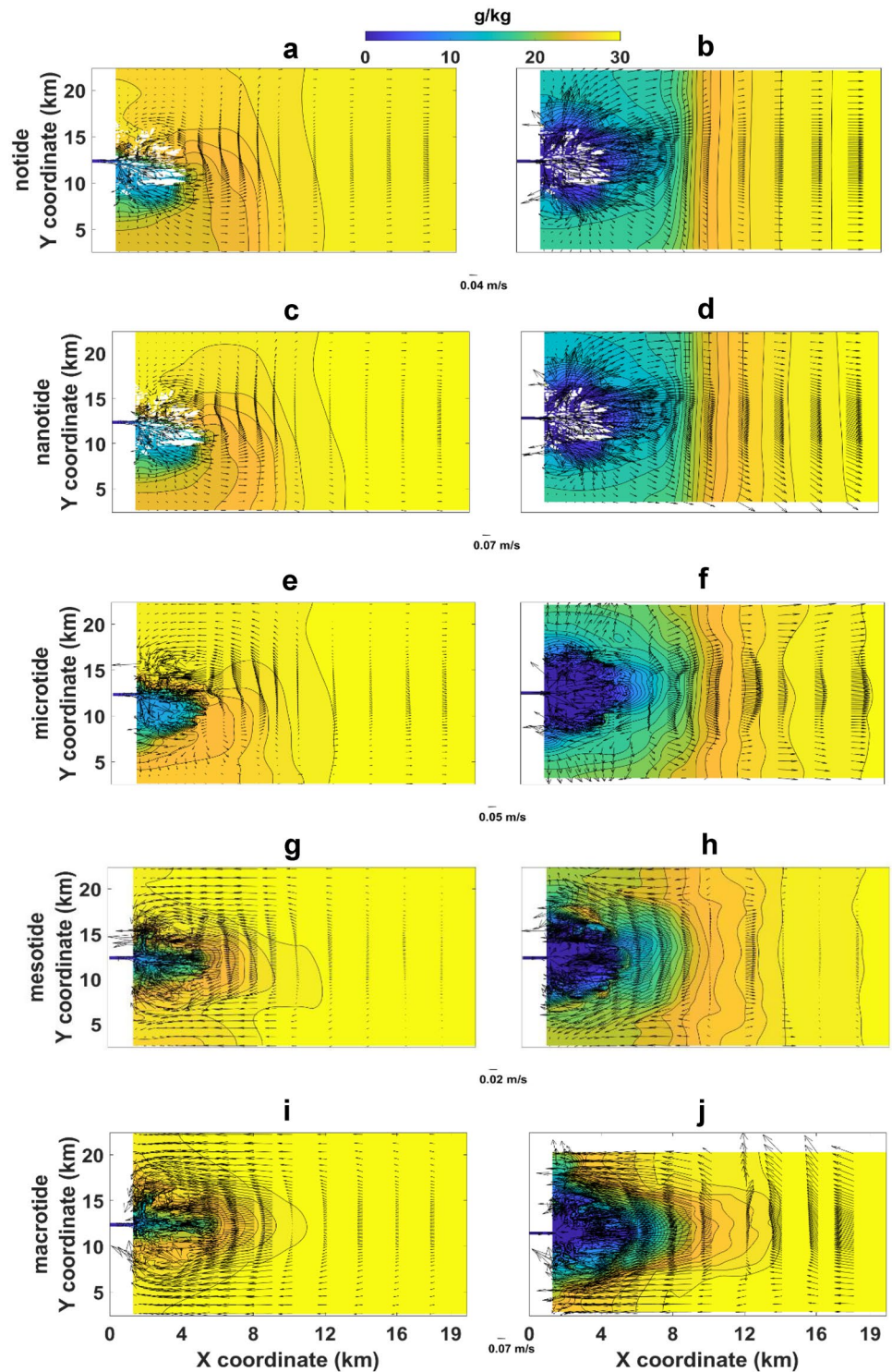
and 3b, d). The tide can also enhance the flow and override the bathymetric control so that a more spatially symmetric salinity distribution is observed at the maps of the tidally influenced cases for both dry and wet season (panels e–j in Figs. 2 and 3). The salinity in the delta is very high during dry seasons. The relevant panels in Figs. 2 and 3(a, c, e, g, i)

show that it barely drops below 10 g/kg in the vicinity of the inlet. This signifies salt intrusion in the river inlet. During the wet season (panels b, d, f, h, j in Figs. 2 and 3), a deep blue-coloured area of low salinity (< 5 g/kg) develops. The more symmetric the distribution becomes, the more constrained are the areas of low water. Table 2 displays the evolution with

the TA of the area with salinity less than 5 g/kg. The area increases progressively with the TA until it reaches the microtide's scenario amplitude (0.15 m). Beyond this threshold, the area decreases as the TA increases so that the macrotide scenario demonstrates the lowest value. Even though the low TA in scenario 2 enlarges the area compared to scenario 1 (no tide), the difference between the two cases is not significant.

In the absence of tides (Figs. 2a, c and 3a, c), the salinity beyond a distance of 10 km from the river boundary reaches sea water values (more than 27 g/kg) at dry seasons. On the contrary, during the wet season, the isohalines are clustered in the vicinity of the bed slope developing sharp horizontal gradients parallel to the bed (Figs. 2b, d and 3b, d). In the presence of tides, the enhanced freshwater flow causes sharper horizontal gradients outside of the delta where an offshore buoyant plume starts to develop.

Flow Variation

The two river-dominated cases exhibit a common feature which is the presence of dry points inside the delta (white-coloured areas in Figs. 2a-d and 3a-d) that lie above the mean water level. In the tidal case (Figs. 2e–j and 3e–j), freshwater is trapped in these areas but remains stagnant as no flow currents develop between these points.

In the river-dominated cases, the high lateral salinity gradients across the inlet observed at dry season have a strong influence on the flow direction. Onshore and offshore flow develops at the high and low salinity areas respectively (Figs. 2a, c and 3a, c). The offshore flow magnitude is stronger since the horizontal salinity gradients are higher in this case. The flow becomes parallel to the offshore boundary at the bed slope following the horizontal salinity gradient orientation (see 'Salinity Variation with Seasonality, Tidal Amplitude and Stage'). During wet season, the flow becomes unidirectional (Figs. 2b, d and 3b, d).

During flood tide (Fig. 3), scenarios 3, 4 and 5 develop different flow patterns at the deep area downstream of the bed slope. In scenario 3, the river discharge prevails over the tidal flow imposing a unidirectional seaward flow (Fig. 3e, f). However, landward flow at the flood tide can still be seen in the shallower area upstream of the slope where the delta lies. The flow direction turns landward at the flood tide with its magnitude increasing as the TA becomes higher (compare flow vectors between Fig. 3g, h and 3i, j).

A better illustration of the flow magnitude increase by the tide can be seen in Fig. 1f. The horizontal velocity in the delta is averaged over depth and space (upstream of the red borderline in Fig. 1b) and over two tidal cycles to get its daily evolution. The velocity magnitude of scenarios 4 and 5 is more than double that of the three others and resembles the shape of the hydrograph (Fig. 1e) with lower values at dry and higher values at the wet season. On the contrary, the first three scenarios exhibit a short period of velocity decrease (increase) in the 1st (2nd) semester. This is a feature that reflects the impact of the bathymetric asymmetry on the flow jet. When the river discharge is low, the cross-flow is downward and the jet turns to the right of the inlet (looking seaward). The jet tends to become symmetric as the river discharge increases in time. During this transition stage between the asymmetric and symmetric flow jets, the cross-flow tends to zero and that causes a decrease of the resultant velocity. With the crossflow almost zero, the total velocity continues to rise following again the hydrograph's shape. The opposite process occurs at the 2nd semester. Figure 1f clearly shows that the simulations are separated in two groups: scenarios 1, 2 and 3 with salinity distribution constrained by the bathymetry while scenarios 4 and 5 remain unaffected. In the rest of the paper, the first three scenarios will be referred as bathymetry-controlled and the two others as non-bathymetry-controlled scenarios.

Intratidal Effect of Tidal Amplitude Variation on the Freshwater Area

In this study, the 2 g/kg isohaline is taken as the limit of the freshwater area (FWA) because this value is generally considered a threshold of impact to human activities and aquatic life (Schubel 1992; Monismith et al. 2002; Andrews et al. 2017). Figures 2 and 3 indicate that during periods of low flows (left column panels) the salinity is much higher than this threshold. As the river discharge increases in time reaching its peak, the salinity decreases and drops below the 2 g/kg threshold at some instant between the minimum (day 1) and maximum flow (day 180). Figure 4 displays the limits of the 2 g/kg isohaline for the five simulations with different TA at the day of the maximum flow (180 days from the start) and at four instances of the tidal cycle: (1) LW, (2) 3 h after LW (MTL_L), (3) HW and (4) 3 h after HW (MTL_H). The area within these limits is defined as the freshwater area (FWA).

The no tide isohaline does not vary within the tidal cycle but is included for comparison. The contour lines of the river-dominated cases (blue and red colour) are interrupted because of the presence of the dry exposed areas (see the white-coloured areas in Figs. 2a-d and 3a-d). In addition, single spots with salinity equal to 2 g/kg appear inside the delta (the blue colour covers the red). These

Table 2 The area (km²) within the 5 g/kg isohaline 3 h after LW (flood) and HW (ebb), 180 days after the start of the simulation

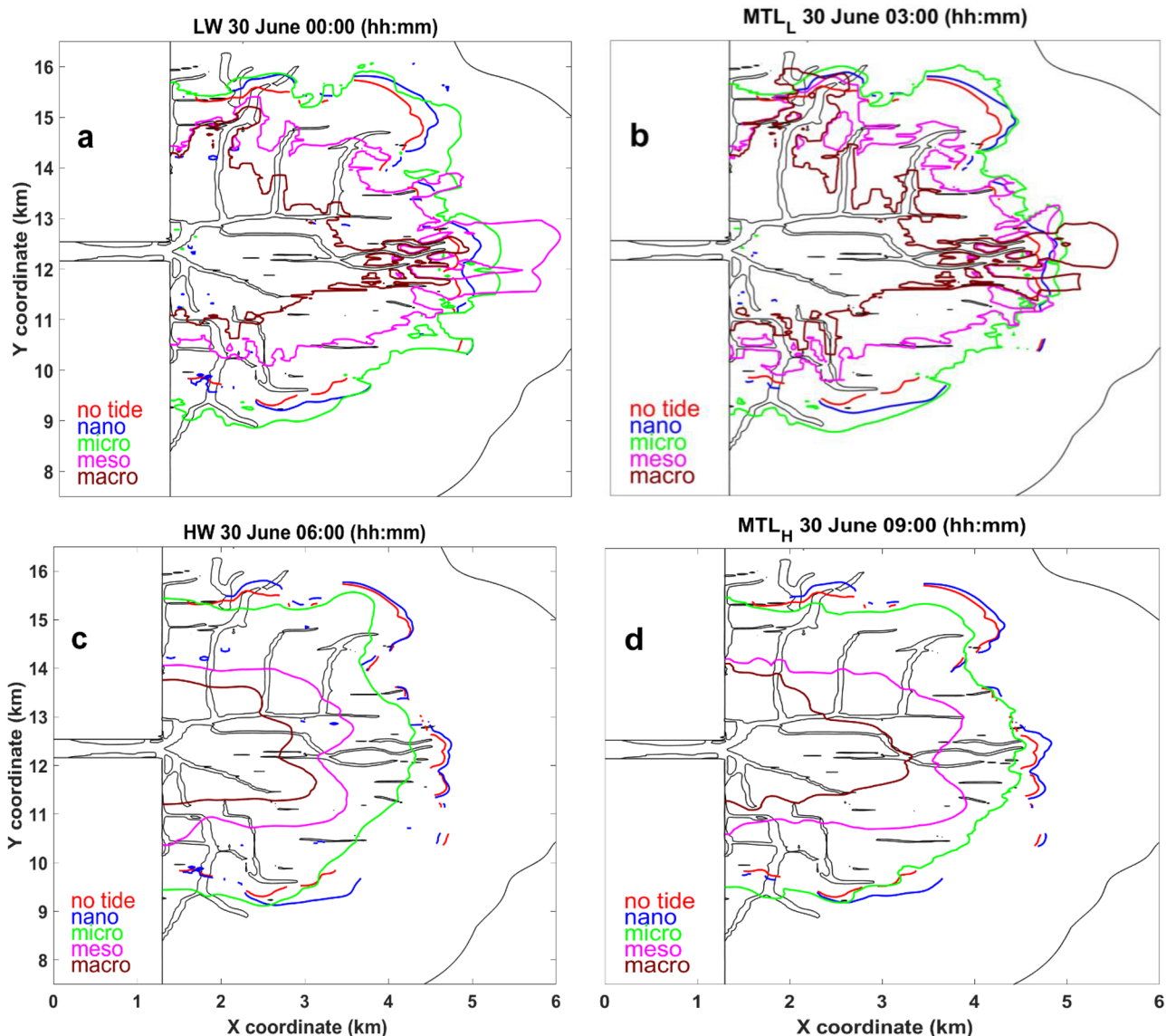| Simulation	No tide	Nanotide	Micro	Meso	Macro
MTL_L	25.51	25.79	31.51	22.75	18.02
MTL_H	25.51	25.57	29.08	16.20	9.60

Fig. 4 The position of the 2 g/kg isohaline for every amplitude 180 days after the start of the simulation at the surface layer and at times of **a** LW, **b** 3 h after LW, **c** HW and **d** 3 h after HW. Colours denote the different tidal amplitudes. The black lines delineate the delta's channels and border with the sea

are most likely caused by 'ponding' where freshwater is trapped around the dry areas. Overall, the FWA shows different patterns between flood (panels a, b) and ebb (panels c, d) tide. The 2 g/kg isohaline is smoother at the ebb tide when both river and tidal flow act seaward. The landward tidal flow during flood tide causes lateral changes to the contour shape while an offshore buoyant plume tends to form in the meso- and macrotide scenarios (Fig. 4a and b). This leads to a wider FWA during flood (top panels) than ebb tide (bottom panels) in every scenario. In addition, it causes a gradual increase to this area when the amplitude rises from 0 m to 0.15 m while at the ebb tide this occurs

only between the two rived-dominated cases (scenario 2 shows higher FWA than scenario 1). Any increase of the amplitude above these thresholds results in a decrease of the FWA. The FWA variation with the amplitude and the tide can be seen quantitatively in Table 3. These results indicate different salinity response to TA changes depending on the tide (flood or ebb).

Finally, at earlier times and during low flow seasons, the limits of this isohaline can be constrained inside the inlet indicating salt intrusion irrespective of the tidal stage. Figure S3 included in the 'Online Resource' illustrates such conditions 30 days after the start of the simulation when the river

Table 3 Freshwater area at times of high water (HW), low water (LW), 3 h before LW (MTL_H) and 3 h before HW (MTL_L) 180 days after the start of the simulation

Simulation	No tide	Nano-tide	Micro	Meso	Macro
LW	16.72	18.30	21.79	14.30	8.27
MTL_L	16.72	18.62	20.95	14.26	10.15
HW	16.72	17.64	15.98	7.28	5.16
MTL_H	16.72	17.94	16.40	8.24	5.54

discharge is still considerably low. This must raise concerns to water management authorities about the impact of sustained drought periods in river deltas.

Vertical Salinity Distribution in the Tide-Influenced Scenarios

The results in 'Horizontal Salinity Distribution and Flow Field Evolution with the Tidal Variation' present the spatial salinity distribution in the horizontal direction and revealed the development of an offshore buoyant plume in the tidally influenced scenarios (Fig. 2f, h, j and 3f, h, j). The plume is the result of buoyant inflow from riverine water entering the delta and has become fully developed at the maximum flow day (~ day 180, 01/07). Figure 5 illustrates the vertical salinity distribution along a transect with start and end points at the upstream ($X = 0$ km) and the bed slope location ($X = 10$ km) respectively following the magenta-coloured

line in Fig. 1b. Figure 5 displays the vertical salinity distribution on the day of the maximum river discharge (180 days from the start, 1st of July) at the times of the maximum velocity during ebb (panels a, b, c) and flood (panels d, e, f) tide.

The starting point of the offshore buoyant plume may be set conventionally at the delta end ($X \sim 5$ km). The 18 g/kg isohaline (light green colour) seems to delineate best the front between the buoyant water and the ambient seawater with salinity more than 20 g/kg (orange and yellow colour). This front is inclined in the microtide scenario at both tidal stages (Fig. 5a, d). The buoyant inflow causes the lower density water to move faster offshore compared to the denser bottom water. This indicates the development of a surface-advected plume. At the ebb tide (Fig. 5a), the isohalines have been tilted and stratification is expected to occur at the end of the ebb stage. On the other hand, the flood tide (Fig. 5d) pushes the isohalines landward in order to destabilize stratification and develops a bottom boundary layer at the front location which is capped by the pycnocline. This resembles what is reported by observations of turbulence in shallow estuaries that are characterized by a well-mixed bottom boundary layer being capped by a stable density gradient in shallow estuaries (Stacey and Ralston 2005). The front location moves further downstream as the velocity increases (i.e. the amplitude increases). As the tidal level increases, tide-induced vertical mixing leads to plume structures that occupy the entire water column. This is very clear in panel c referring to the macrotide scenario. The mesotide scenario

Fig. 5 The vertical salinity distribution through the delta along the transect denoted by the magenta colour line in Fig. 1b for the three tide-influenced scenarios. Left panels correspond to microtide (0.15 m), middle panels to mesotide (0.56 m) and right panels to the macrotide scenario (1.1 m). Results are presented on the day of maximum flow, 180 days from the start of the simulation and at the time of the maximum velocity during the ebb **a**, **b**, **c** and flood **d**, **e**, **f** tide
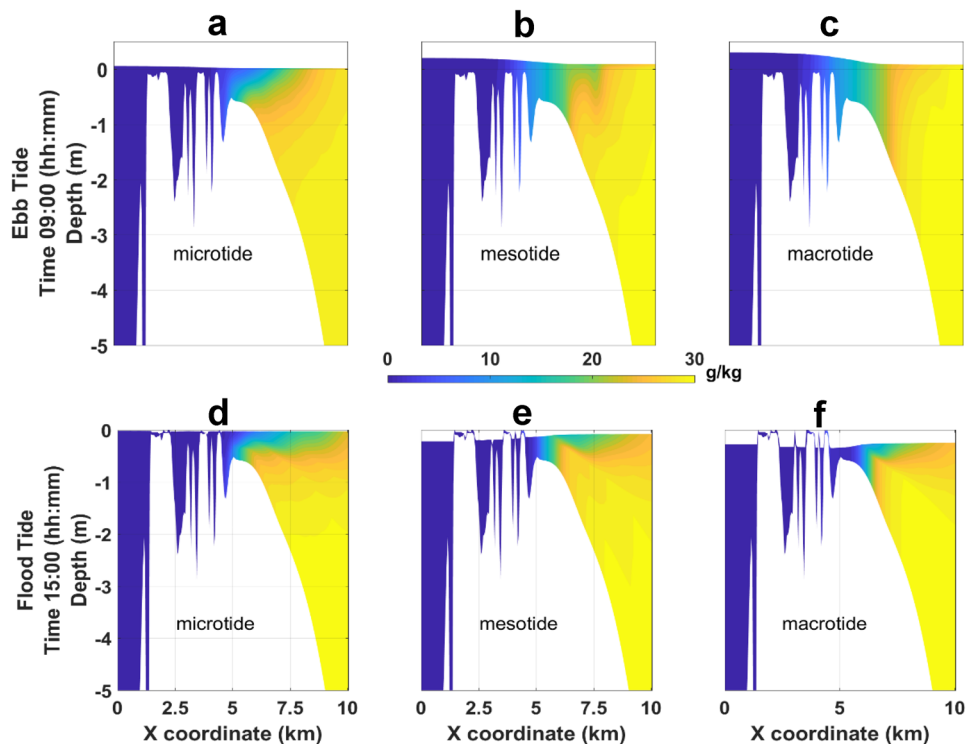
(Fig. 5b, e) seems to develop an intermediate plume type between those of the microtide (surface advected) and macrotide (bottom advected). While the plume is in contact with the bottom for some distance, it is detached further downstream where it keeps moving offshore with its front closer to the surface. This is more pronounced at the flood tide (Fig. 5e) because the counteraction between landward tidal and seaward river flow tends to lengthen the plume at the surface (see also Figs. 2h and 3h). Something similar occurs at the macrotide case (Fig. 5f) with the surface layer being deeper in this case since the macrotide bottom-advected plume reaches higher depths. Conclusively, a tidal amplitude increase may convert progressively a surface-advected to bottom-advected plume. In addition, it results in a further offshore front displacement.

Alongside the buoyant plume structure, Fig. 5 gives also an image of the FWA length along this section which is denoted by the dark blue colour. This length is seen to decrease with the amplitude increase before the LW time (ebb tide, panels a, b, c) reflecting the influence of higher tidal prisms on the delta's salinity. On the contrary, it increases with the amplitude in an instant during flood tide probably because the higher tidal flows cause a lengthening when acting against the river flow similarly to what happens with the plume's length at the same times.

Freshwater Volume Evolution in Time with the Tide Amplitude

To get an overview of the tidal variation impact on the freshwater conditions, the freshwater volume (FWV) of the delta (area upstream of the red borderline in Fig. 1b) is calculated.

FWV is defined as the product of a segment's freshwater fraction times its volume. Considering the grid cells of the idealized model as segments, FWV is calculated by the following equation (Alber and Sheldon 1999):

$$\sum_{i=1}^{n}\left[\left(\frac{S_0 - S_i}{S_o}\right) * Vol_i\right] \tag{5}$$

where n is the number of grid cells, S_o is the oceanic salinity equal to 30 g/kg, S_i is the depth averaged salinity of a grid cell i and Vol_i its volume. Figure 6 depicts the evolution in time of the FWV for the various amplitudes and at the times of maximum (HW, panel a) and minimum (LW, panel b) water volume in the delta. The calculation in Eq. 5 is done by introducing the salinity values at the times of HW and LW of the first tidal cycle of the day. The FWV evolution follows the hydrograph's shape (Fig. 1e) with maximum values at periods of high and minimum at periods of low flows. The FWV curves are affected by the shape of the spatial salinity distribution ('Salinity Variation with Seasonality, Tidal Amplitude and Stage' and 'Flow Variation'). The rate of FWV increase (1st semester) or decrease (2nd semester) changes when the spatial distribution transforms from an asymmetric to symmetric shape and vice versa. This is more obvious in the three bathymetry-controlled scenarios (1, 2 and 3). The time instants of these changes agree with the corresponding changes of velocity magnitude in Fig. 1f. Therefore, the FWV curves are not symmetric with respect to their peak because the spatial distribution remains symmetric more time in the 2nd semester due to the salinity's slower response to decreasing river discharges (Savenije 2005).
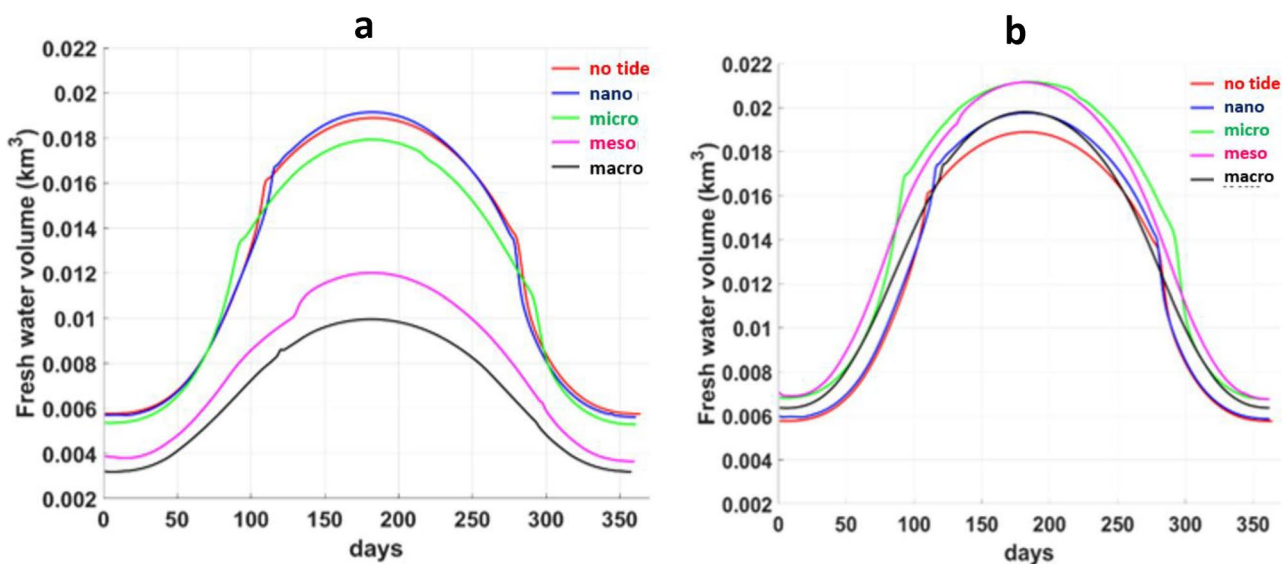

Fig. 6 Daily evolution of the freshwater volume in the delta for each scenario at times of **a** HW and **b** LW for the first tidal cycle of the day
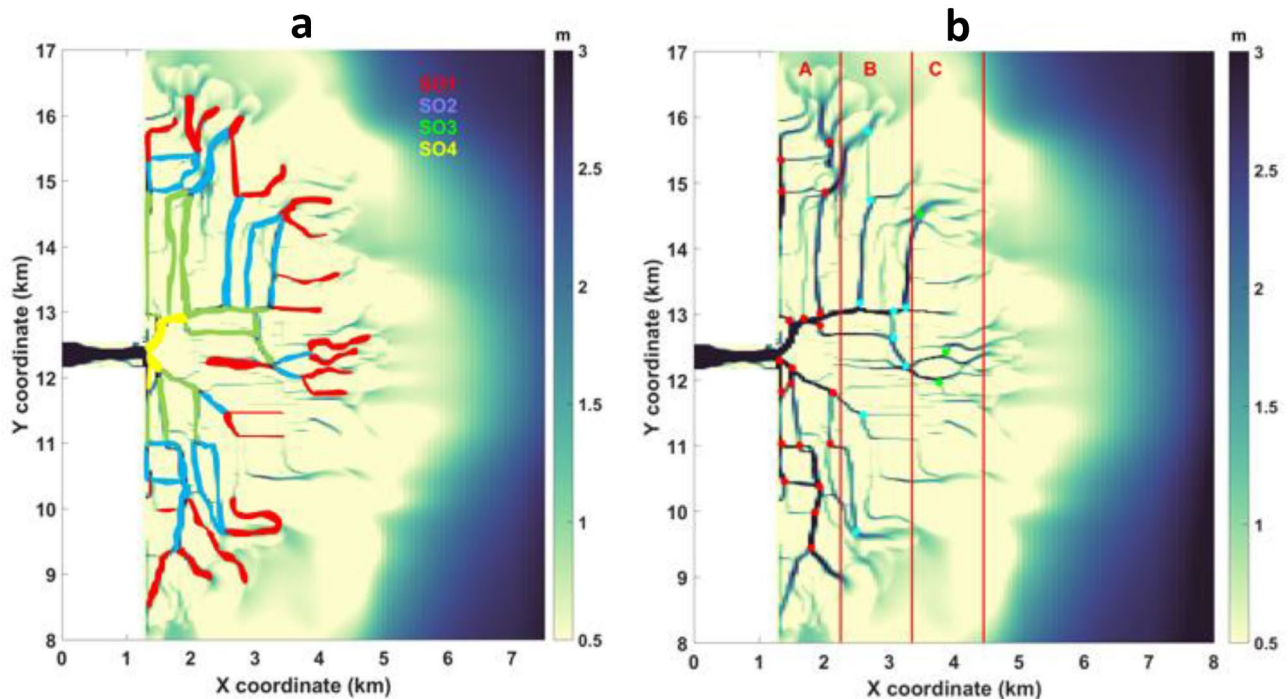
Fig. 7 a A sketch of the delta with the channels coloured by their stream order (SO) number. First order corresponds to branchless channels. The SO increases upstream at every junction between channels of equal order. **b** Schematic representation of the width function method. The junctions between delta channels are denoted by coloured circles. Each colour corresponds to a different generation group that is limited between the vertical lines A, B and C. The lines are drawn with a step of 1.1 km between them. The generation A line is drawn 1.1 km from the shore. The width of a generation equals the number of the coloured circles per generation group. According to this, the width of A, B and C is 20, 9 and 3 respectively

At HW times (Fig. 6a), FWV of the three bathymetry-controlled scenarios is higher than the two others at all times. The FWV of the two river-dominated scenarios is almost equal during the entire simulation period. At the wet season, when the high river discharge increases mixing, the difference between the river and tidally influenced cases becomes larger.

At the ebb tide, an amount of sea water leaves the delta while river discharge still flows in it. For this reason, the FWV is higher for every scenario (except for the no tide case) at times of LW (Fig. 6b). The tidal cases exhibit higher FWV than the river-dominated ones. The reason is that in the absence of tides (and thus tide-induced mixing), the river discharge does not manage to reach downstream areas very far from the inlet where the water remains either partially mixed or stratified. The difference becomes larger at high flow periods (wet season) when combined tidal and freshwater flow usually increase mixing. This does not concern scenario 5 (maximum TA = 1.1 m) where the FWV increase during wet season is limited so that it is equalled by FWV of scenario 2. Interestingly, microtide and mesotide scenarios have comparable FWV at most times and an equal maximum occurring in the middle of the year (day 180, 1st of July).

According to these results, a TA increase will most likely have different effects on the delta's salinity between HW and LW. Significant decrease can be expected at HW. On the other hand, tidal level increase could be beneficial to some extent at LW.

Relation Between Salinity and Delta's Bifurcation

Stream Order The delta channels are classified and assigned a stream order number (SO) according to the Strahler–Horton method (Strahler 1952) as presented in Fig. 7a. To exclude low lying regions of the delta plain, channels shallower than half a metre were not considered. Independent channels disconnected from the main network were also neglected. By this, 57 channels were identified and classified. This idealized delta has a 4th-order bifurcation (four stream orders). Branchless channels are of first order. The order increases upstream when two channels of equal order make a junction. If a channel meets with another channel of lower order, its order does not change. Then, the mean over depth salinity is averaged within channels of equal order. The result is further averaged over two tidal cycles to get daily values of the mean per SO salinity. Figure 8a-c show the evolution in time of these averages per SO for

scenarios 1, 3 and 5 (TA = 0 m/0.15 m/1.1 m respectively). The same plots for scenarios 2 and 4 can be found in the 'Online Resource' (Figure S2 A and B). Figure 8c exhibits a clear trend with salinity increasing as the SO decreases at all times. On the contrary, this trend is present only at periods of high flows (wet season) in Fig. 8a and b where the various orders overlap each other at the start and the end of the year and do not follow a constant succession. The stream orders in Fig. 7a expand in space in a somehow semi-circular or symmetric manner so that SO1 channels are located at the end of the delta and SO4 close to the river inlet. It seems then that the trend of increasing salinity with decreasing SO does not apply for the bathymetry-controlled scenarios when the spatial salinity distribution is not symmetric.

The bathymetry effect is overcome with the flow enhancement by the TA increase (Fig. 1f). In Fig. 8a (no tide), the first three orders overlap with each other while in Fig. 8b (TA = 0.15 m) only the two first orders do overlap. With the TA increase, the system moves progressively from a state of no symmetry to a symmetric one where the salinity–SO correlation applies again. It looks like the correlation with the stream order applies better to symmetric salinity distributions.

Width Function Since the SO rule was not successful for periods with no symmetric salinity distribution, an alternative solution is needed to relate salinity to the delta's bifurcation. Other stream labelling methods (e.g. Horton, Miller-Oiller, Scheidegger) do not serve this purpose because they follow a procedure of channel ordering very similar to the Strahler–Horton. Nevertheless, the width function (WF) offers the opportunity to summarize the delta's bifurcations in terms of channel links rather than the channels themselves (see 'Introduction'). It is adapted then for the present idealized delta model. The delta network is divided into three areas by three vertical lines of equal distance (1.1 km) between them (Fig. 7b). These lines are drawn starting from the delta apex and until the end of the delta where there are no other junctions. For the width function method to be applicable, its distribution in space must exhibit a certain skewness (positive or negative). With the current space step, a positive skewness appears with the number of junctions reducing downstream as the delta's cross section does. In the following text, the three vertical lines (A, B and C Fig. 7b) are referred as generations following Kirkby (1976). The width of each generation is the number of junctions between two successive generations. For example, the width of generation B is the number of junctions between the borderlines of generation B and A. The width A is the number of junctions between generation A and the vertical line crossing through the delta apex (X = 1250 m). Figure 8d, e and f show the evolution in time of the mean over depth salinity averaged within channels belonging to the same

generation for scenarios 1, 3 and 5 (TA = 0 m/0.15 m/1.1 m respectively). Results for scenarios 2 and 4 can be found in the 'Online Resource' (Figure S2 C and D). The salinity is averaged again within two tidal cycles to get daily values. It is observed that the range of the lateral averages in the WF figures is much smaller than that of the radial averages in the SO ones because channels far from the delta apex and closer to the lateral boundaries are included in every generation increasing these averages. The results show that SO and WF methods may be complementary. In Fig. 8d (no tide) and e (microtide), salinity decreases with the width increase only for low flow periods while in Fig. 8f (macrotide) this happens at all times. There is an indication that when the SO method is not applicable the WF can be and vice versa.

Freshwater Conditions Duration in Space Taking a salinity equal to 2 g/kg as a freshwater threshold value (see 'Intratidal Effect of Tidal Amplitude Variation on the Freshwater Area'), the SO and WF methods could be used in order to determine an indicative time that the water in the delta remains fresh (i.e. the average salinity is < 2 g/kg) in each scenario. Figure 9 illustrates the number of days that the mean over depth salinity remains below 2 g/kg when averaged within channels of the same SO (panel a) and within the same generation (panel b). Both figures project a spatial image of the time that freshwater conditions prevail based on a radial (Fig. 9a) and lateral (Fig. 9b) averaging. In Fig. 9a the freshwater conditions duration (FWD) increases in every scenario upstream as the SO does too. FWD rises too as the TA increases from 0 m to 0.15 m. However, this positive effect does not concern channels of SO3 and 4 of scenario 2 (TA = 0.02 m) that lie close to the inlet and are subject to limited influence from the low tidal level of these scenarios. Within the three tidal cases, the FWD reduces with the TA increase.

Figure 9b shows a common order between generations for every scenario (i.e. B > C > A). However, the lateral salinity averages in scenarios 4 and 5 do not fall below 2 g/kg at all. This indicates that in the case of very high amplitudes, the freshwater does not reach distant areas laterally and any influence from the river flow is mainly transmitted longitudinally. A paradox is that FWD is minimum in generation A (GA) which is the closest to the delta apex (Fig. 7b) and is also smaller than that of generation C (GC) which is the most distant section. The reason is the delta width which is the maximum in GA (equal to 20) and the minimum in GC (equal to 3). This means that GA is the longest section including areas with higher salinity in large lateral distances from the river. On the other hand, GC covers the smallest delta section and thus salinity averages are lower. Consequently, the delta remains fresh for longer periods within the borders of generation B where the delta has its medium width equal to 9.
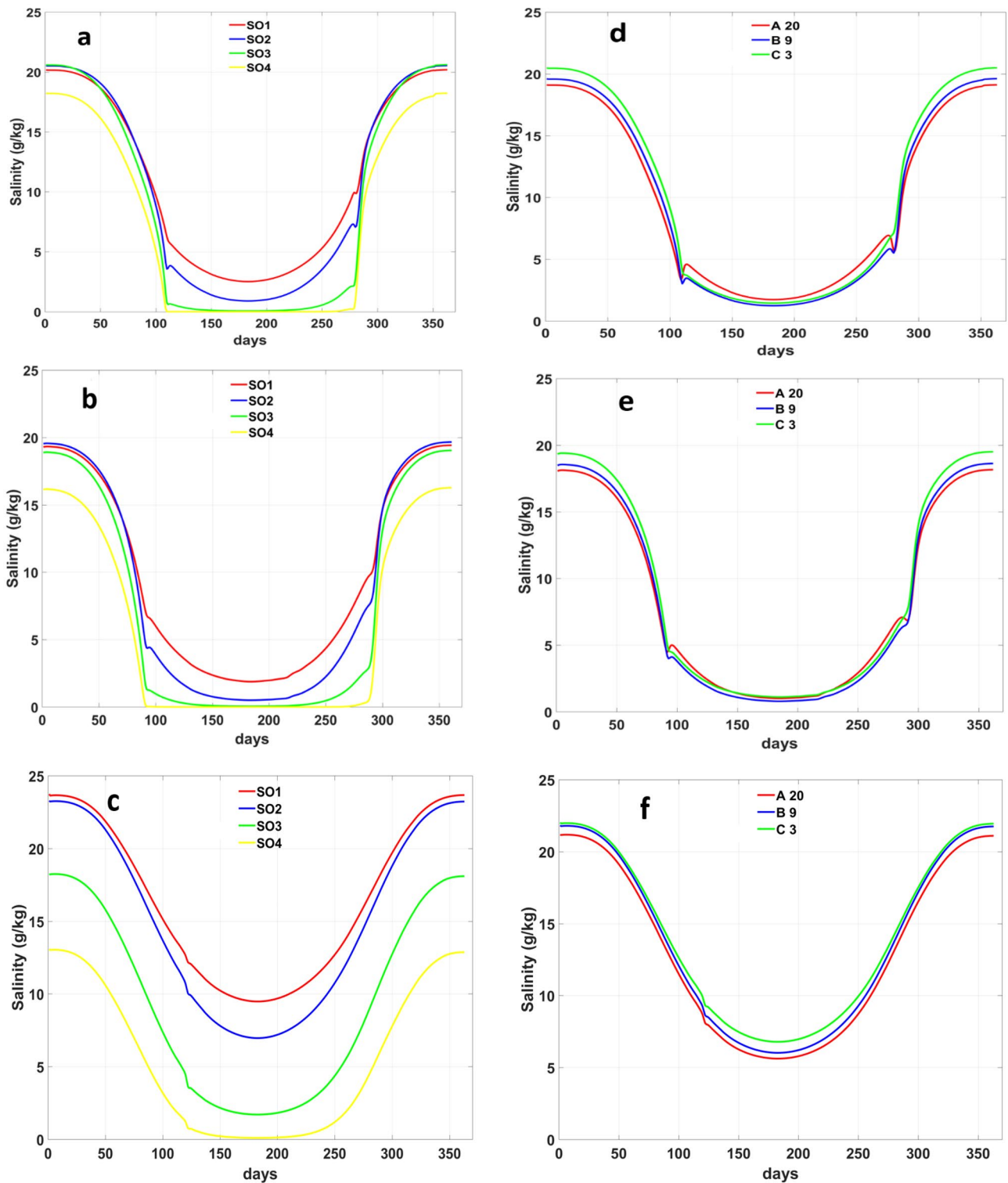
Fig. 8 The evolution in time of the mean over depth salinity averaged within channels of the same stream order in **a** no tide, **b** microtide and **c** macrotide scenarios. The evolution in time of the mean over depth salinity averaged within channel branches of a generation group in **d** no tide, **e** microtide and **f** macrotide scenarios
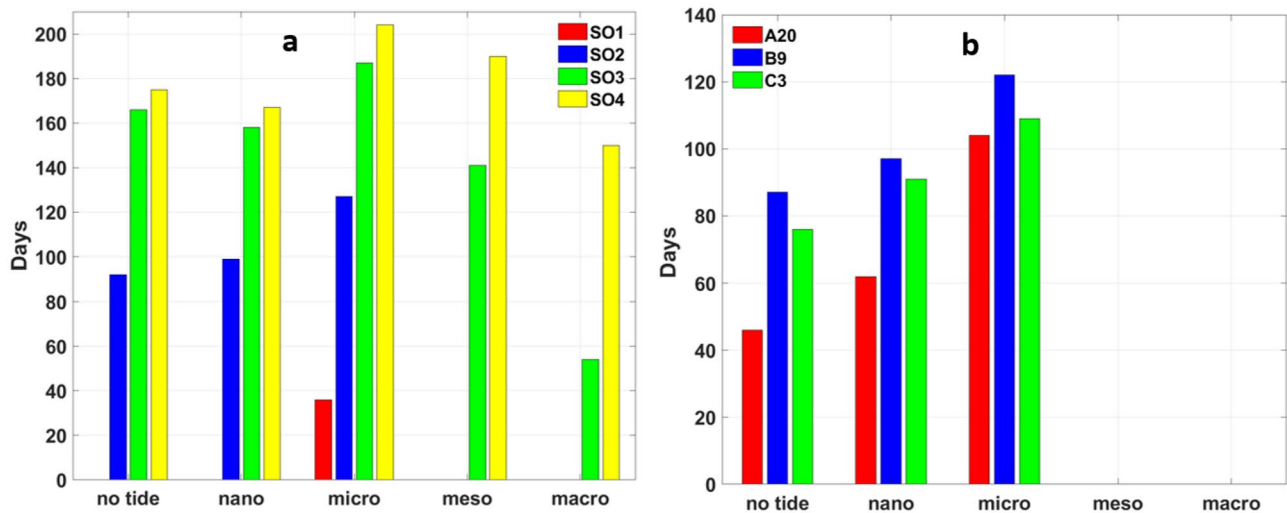
Fig. 9 The time in days that the depth averaged salinity remains below 2 g/kg when averaged within channels of the same **a** stream order and **b** generation group. In order to obtain daily values, the salinity is averaged over two tidal cycles

The microtide scenario emerges in both methods as the one with the longest freshwater period at every order and generation. It is also the only case where even the very distant channels of SO1 become fresh at least for some time (Fig. 9a). The calculation of the FWD based on radial and lateral salinity averages may provide some useful conclusions by combining their results. For example, the SO3 channels that become fresh during wet season for 140 days in e.g. scenario 4 (Fig. 9a) are most probably only those located in straight distance from the inlet and not sideways (Fig. 7a) since scenario 4 does not exhibit any results for lateral averages in Fig. 9b. In addition, it seems that the delta's cross-section size may indicate areas of high or low salinity.

Relation Between Salinity and River Discharge

Building on Matsoukis et al. (2021) where an at-the station relationship between salinity and river discharge was developed, the existence of the exponential salinity (S)–river discharge (Q) relation in the presence of tides is further investigated. The depth-averaged salinity is radially averaged over a semi-circle with its centre at the delta apex (Fig. 1b). Figure 10 a and b show the daily variation between the radially averaged salinity and river discharge for each scenario. Since the hydrograph is symmetric, data for the first semester are used only. A regression analysis between S and Q verifies an exponential relation for high amplitudes (Fig. 10b) which can be justified

by both the very high R^2_2 coefficients and the fitting curves denoted by black colour.

In contrast, the S–Q curves in Fig. 10a indicate the existence of a flow threshold which determines two different regimes for the S–Q relation. It was found that below a threshold tidal range, salinity and river discharge are better correlated by a double exponential equation in the following form:

$$S = \alpha_1 * e^{\beta_1 Q} + \alpha_2 * e^{\beta_2 Q} \qquad (6)$$

with $\alpha_1 < 0, \alpha_2 > 0, \beta_1 > 0, \beta_2 < 0$. The theory behind Eq. 6 is further discussed in 'Salinity–River Discharge Relationship'. The parts of the S–Q curves that are better fitted by Eq. (6) are extracted from Fig. 10a and presented separately in Fig. 10c. The included fitted curves (in black colour) and the high values (close to 1) of the R^2 coefficients support the assumption of a double exponential fitting. The value of the flow threshold determining the nature of the fitting equation varies with the TA in Fig. 10c. This depends at the moment the spatial distribution changes from an asymmetric to symmetric distribution. Since this happens earlier in scenario 3 and later in scenario 2 (Fig. 1f), the flow threshold is higher in the latter and lower in the former. Above the threshold, the S–Q distribution returns to a single exponential form.

The reason for the difference in the S–Q distribution between the high (scenarios 4 and 5) and low amplitude cases (scenarios 1, 2 and 3) is the bathymetric asymmetry but this is discussed in more detail in 'Salinity–River Discharge Relationship'.
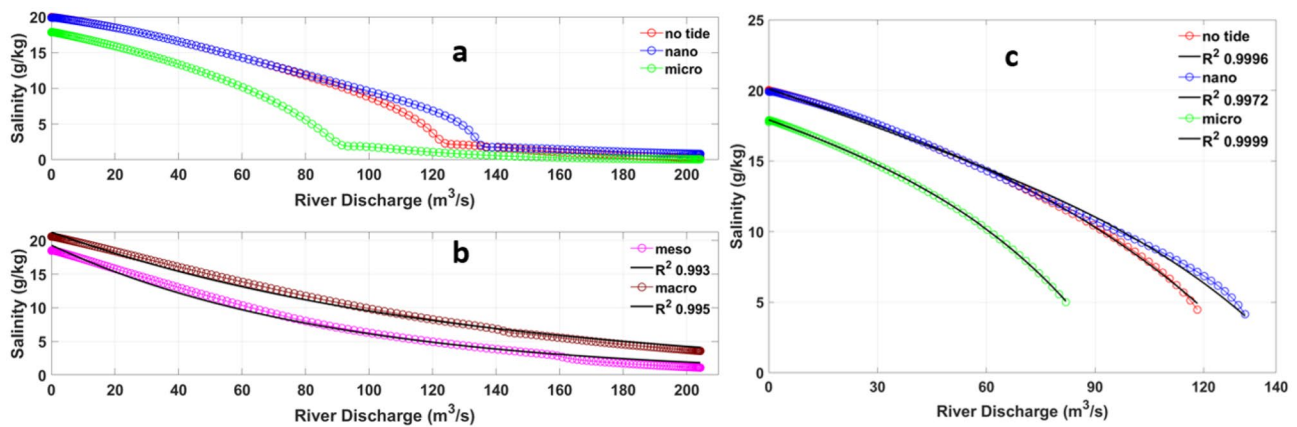
Fig. 10 Daily averages of the depth averaged salinity averaged over the SS' semicircle shown in Fig. 1b against the daily river discharge (Fig. 1f) for **a** scenarios 1, 2 and 3 and **b** scenarios 4 and 5. The black lines in panel **b** are the fitting curves after a regression analysis for a single term exponential equation. The R^2 coefficients for an expo- nential fitting are included in the legend. **c** The salinity (S)-river dis- charge (Q) curves of panel a cut for a shorter period during which the two magnitudes seem to have a very good fit for a double exponential equation. The R^2 coefficients for the double exponential fitting are displayed in the legend

Discussion

Impact of the Tidal Amplitude Variation on the Salinity Distribution

The presence of tides in the system may have several posi- tive effects. For example, when the river discharge is low (dry season), the riverine flow may not be able to transfer freshwater in long distances leaving the downstream parts of the delta with high salinity. Tide-induced mixing though can decrease the salinity in these outer areas. This is the reason why the FWV is higher in the tidal cases at the times of the minimum water level (LW) compared to the river-dominated cases (Fig. 6b). However, these positive effects may reverse if the TA increases too much and starts decreasing the FWV (Fig. 6a). Results indicated that low tide systems may ben- efit by a TA increase while high tide–dominated systems will not. In the latter case, a decrease of the TA due to SLR could be beneficial for such systems. Within the context of this manuscript, the microtide case (scenario 3, TA = 0.15 m and flow/tide ratio equal to 0.073) represents the bound- ary between river-dominated and tidally influenced cases. The TA increase from 0 m to 0.15 m results in wider low salinity areas (Tables 2 and 3) and leads to more symmetric spatial salinity distribution (Figs. 2 and 3). Therefore, the microtide case provides wider areas of low salinity (< 5 g/ kg) and freshwater (< 2 g/kg) and keeps the delta fresh for the longest period (Fig. 9). In contrast, further increase of the TA resulted in a significant reduction of the low salinity areas, freshwater periods and volumes in the delta.

Tidal motion imposes several mechanisms on buoyant inflow. Garvine (1999) identifies enhanced vertical (tidal)

mixing, tidal straining and subtidal flow nonlinearities as some of them. These may be the cause behind the differences in the spatial salinity distribution due to TA variations. At low flow times (panels a, c, e, g, i in Figs. 2 and 3), freshwater flow is directed to the right of the delta apex decreasing the salinity but leaving almost unaffected the areas left of it. The TA increase leads to more symmetric shapes (compare between panels a, c, e and g, i in Figs. 2 and 3). Such a tidal effect has been observed on buoyant plumes deflected to the right under the influence of the Coriolis force (in the northern hemisphere) or in the presence of ambient crossflows (Chao and Boicourt 1986; Chao 1988; O'Donnell 1990; Oye 1992; Kourafalou et al. 1996; Narayanan and Garvine 2002; Lee and Valle-Levinson 2013; Cole and Hetland 2016). Since none of these parameters is included in these simulations the asymmetry in the present case can only be ascribed to the bathymetry (see 'Initial Con- ditions'). Many plume studies argued on the effect of high tidal forcing that diminishes such deflections. Chao (1990) has stated that the tidal residual circulation enhances the plume growth and limits the coastal jet. Garvine (1999) noticed that tidal forc- ing restricts the plume advection in the across-shelf direction decreasing significantly the upshelf and downshelf penetration. This tidal effect towards more symmetric plumes is a common conclusion in a number of other papers concerning buoyant plume structures under tidal influence (Chao 1990; Isobe 2005; Guo and Valle-Levinson 2007; Lee and Valle-Levinson 2013).

At high flow times (panels b, d, f, h, j in Figs. 2 and 3), the TA increase constrains the size of the low salinity area (blue coloured with salinity less than 5 g/kg) but causes also the development of an offshore buoyant plume. The plume lengthens at flood tide (Fig. 3) when tide acts landward and river flow seaward. The freshwater plume develops a

density front with important dynamics such as flow non-linearities and influences the shelf circulation at the bottom boundary layer (Csanady 1984; Wright 1989; Chapman and Lentz 1994). Increases of the inflow velocity move the front farther downstream (Yankovsky and Chapman (1997) and this can be seen in the results of Fig. 5. The frontal location moved downstream as the amplitude increased because the flow becomes stronger in this case. Many of the features in Fig. 5 may imply tidal straining effects. Simpson et al. (1990) talk about a distortion of the initially vertical isohalines at the start of the ebb that are later distorted by differential displacement. The isohaline tilting in Fig. 5a probably reflects this kind of distortion under the effect of advection from buoyant inflow. This process is expected to reverse at the flood tide that acts in favour of mixing and destabilizes stratification (Fig. 5d). This kind of effects is less visible in the meso- and macrotidal cases because a different type of plume is developed that comes in contact with the bottom for a certain length. Yankovsky and Chapman (1997) studied the buoyant plumes vertical structure and classified them as surface or bottom-advected. In the latter, the plume occupies the entire water column and the density front extends from the surface to the bottom. In the former, the plume is confined in a thin layer close to the surface and spreads offshore having no contact with the bottom. They identified also a third plume type in an intermediate stage between surface and bottom advected. In this case, the plumes spread offshore in contact with the bottom but beyond some distance the upper part of it detaches from the bottom. It is generally considered that higher tidal amplitudes act in favour of bottom-advected plumes while stronger river discharge tends to stratify the water column developing surface-advected plumes (e.g Yankovsky and Chapman 1997; Guo and Valle-Levinson 2007). The results in 'Vertical Salinity Distribution in the Tide-Influenced Scenarios' indicate a progressive plume conversion from surface to bottom advected as the TA increases. From the three tidally influenced scenarios, the lower amplitude simulation (scenario 3) develops a surface-advected offshore plume irrespective of the tidal stage (Fig. 5a, d). Plumes of this kind may cause stratification and anoxic conditions at the bottom layers and low oxygen can have environmental consequences to the aquatic life (Chant 2012). For example, riverine waters are responsible for recurrent summertime hypoxia at the bottom waters of the river-dominated Mississippi Delta (Schiller et al. 2011). In this context, the microtide amplitude is not so beneficial because contaminants (e.g. organic matter, pesticides, toxic chemicals) from activities such as municipal wastes, industry and agriculture are trapped decreasing the water quality.

Figure 5b and e indicate that the mesotide scenario develops an intermediate plume that lifts off in a certain distance from the delta end. Atkinson (1993) mentions similarities between the depth of detachment and the depth of maximum flow jet penetration. The plume liftoff occurs in a distance of approximately 6 km from the river boundary where the bed starts to deepen. At this site, it is not hydraulically possible anymore for the freshwater flow to be any deeper (Atkinson 1993). The detachment depth is shorter at the flood tide because of increased entrainment (mixing) (Atkinson 1993; Chen and MacDonald 2006). However, this also reduces the salinity in the detached part of the plume (Fig. 5e). The thickness of this detached plume layer is higher in the macrotide scenario (Fig. 5f) probably due to the higher tidal flow even though its length at the surface is shorter.

Impact of Tides and Bathymetry on the Salinity Distribution

Stream Labelling and Bifurcation Methods

Implementation of the Strahler–Horton scheme in an idealized river-dominated delta (Matsoukis et al. 2021) has previously revealed a trend for salinity to increase as the SO decreases. The existence of this trend in systems including tides was tested in this paper. The tide does not seem to modify this relationship as the same trend between salinity and SO is observed in Fig. 8c (macrotide case). Instead, the bathymetry was identified as a factor that influences and prevents this correlation. Because the number of orders presents a symmetric distribution in the delta (Fig. 7a), the salinity does not increase monotonically with the SO decrease when its spatial distribution is not symmetric. At these times, the width function scheme proved to be a useful alternative. In this case, lateral instead of radial salinity averages lead to a similar relationship with salinity decreasing as the width increases. This is very convenient since the two methods appear to be complementary to each other. If the salinity does not decrease with a SO increase, it does decrease with the width increase and vice versa. In addition, the WF seems to provide a trend with salinity when the river discharge is low while the SO applies better at high flows.

The duration that each method (SO or WF) provides a trend and the time of interchange between them might be important to know because it can be indicative of the duration of low and high flow periods, the threshold values between them and the shape of the spatial salinity distribution. Figure 11 gives a timeline of the period and duration that each method provides a trend with salinity in the five scenarios. The timeline shows that a salinity–SO relationship is present for the entire simulation period in the mesotide case (TA = 0.56 m) while both SO and WF methods provide a trend at all times in the macrotide case (TA = 1.1 m). A conclusion can be drawn here because it seems that high amplitude scenarios develop salinity distributions that satisfy both methods independent of seasonal flow variations. Therefore, the discussion about

Fig. 11 A timeline that shows the number of days that salinity decreases with the increase of the stream order or the delta's width (width function) against the tidal amplitude implemented in each scenario. Salinity decreases with the stream order increase during the entire simulation of the mesotide scenario. The salinity decreases with both the stream order and width increase during the entire simulation of the macrotide scenario (black bar)
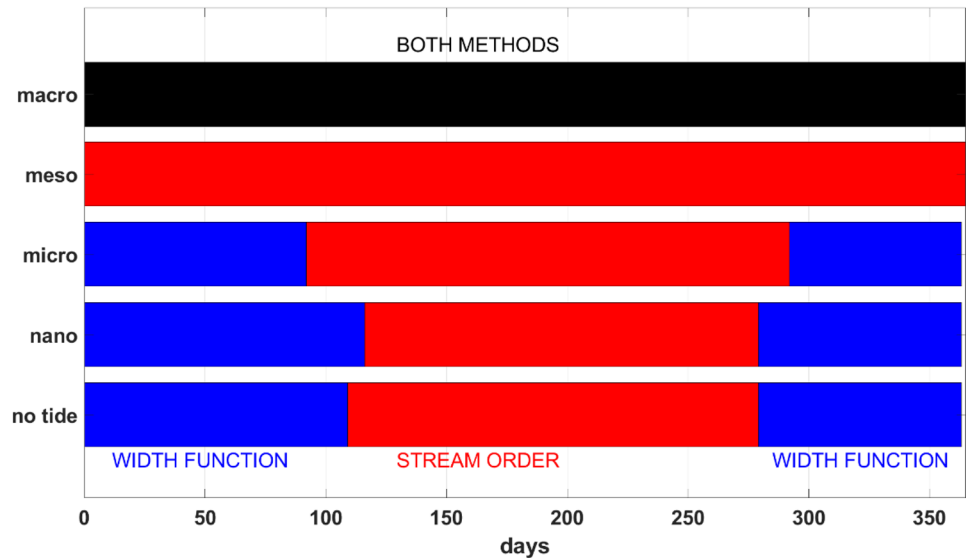

Fig. 11 is limited to the three bathymetry-controlled scenarios that demand the use of the two methods at different periods for a correlation between salinity and delta's geometry.

In the 1st semester, the WF implemented at low flow periods provides a correlation with salinity for 90 days in the microtide case. It remains valid though for longer times in scenario 1 (109 days) and scenario 2 (116 days). The 1-week difference between the two river-dominated scenarios means that the spatial salinity distribution becomes symmetric 1 week later in scenario 2 than in scenario 1. This agrees with Fig. 1f that shows 1-week difference at the time moments the velocity starts to increase before the peak flow (see 'Flow Variation'). That the velocity starts to increase after a short break is indicative that the flow has become symmetric. Notice also that in the 2nd semester the velocity starts to fall (after a short break) at the same time for these two scenarios (281 days after the start). Figure 11 shows that the SO ceases to give a correlation with the salinity at the same time for both river-dominated cases (also 281 days after the start). This correspondence between the times that the delta's velocity magnitude changes and the times of interchange between SO and WF correlations exists in the microtide case as well. The microtide case exhibits a salinity–SO relationship for the longest period compared to the river-dominated cases which is not a surprise knowing that the freshwater period associated with relatively higher flows is longer in scenario 3 (Fig. 9).

Salinity–River Discharge Relationship

The analysis in 'Relation Between Salinity and River Discharge' tested the existence of an S–Q exponential relation in every scenario following the work by Matsoukis et al.

(2021). The authors argued also that the exponential solution in this case approximates solutions of the 1D advection–diffusion equation under certain theoretical assumptions which are also exponential. It should be noted that this is an at-the-station instead of a typical along channel relationship often presented in the literature where the longitudinal salinity is considered (Savenije 2005; Nguyen and Savenije 2006; Nguyen et al. 2008). The tide does not seem to modify this correlation as it can be seen in Fig. 10b for the mesotide and macrotide cases. However, Fig. 10a shows a different kind of distribution between S and Q for the bathymetry-controlled scenarios. Instead of the tide, the bathymetry does influence the S–Q relation as it does in the salinity–SO relationship. A regression analysis indicates that the depth and radially averaged salinity in the delta can be better approximated by an exponential equation with two terms (Eq. 6). This equation could also be a solution of the 1D advection–diffusion equation but for different boundary conditions.

The much deeper channel on the left of the delta apex (Fig. 1b) causes a significant decrease of the flow velocity compared to the rest of the delta and impinges the spreading of freshwater beyond of it. In fact, it acts as a flow boundary. Fischer et al. (1979) presented a series of analytical solutions of the diffusion equation under several initial and boundary conditions. They considered the case of a mass concentration spreading in a 1D system where there is a wall at some distance preventing the flow beyond of it. In this case, the solution is a double exponential equation which is the outcome of the superposition of the real solution (single term exponential) plus an imaginary one that would be the solution if the wall was not present. It seems that the fitting equation (Eq. 6) is similar to this theoretical case. Equation 6 can be divided in two parts as follows:

$$S = A + B$$
$$A = \alpha_1 * e^{\beta_1 Q}, A < 0, \beta_1 > 0 \qquad (7)$$
$$B = \alpha_2 * e^{\beta_2 Q}, B > 0, \beta_2 < 0$$

In the original theoretical case of a wall, the two terms A and B are positive and their exponent coefficients negative so that the concentration of the pollutant increases in front of the wall. The present case is slightly different because the deeper river branch is not impermeable and fixed as a wall would be. Freshwater flows through the channel and downstream of it but not in a constant rate. The salinity is under the influence of two parameters: the freshwater flow that decreases the salinity and the deeper channel that delays this process. The latter influence weakens in time while the former is enhanced. The signs of the exponent coefficients in Eq. 7 indicate that A is a growth and B a decay term. It can be inferred then that the negative term A represents the river discharge influence and the positive term B that of the deep channel that delays the rate of salinity decrease for some time. When the river discharge exceeds a threshold overcoming the deep channel's influence, the S–Q relationship returns into a single exponential form.

An interesting finding is that these flow thresholds are equal in each case with the flow at the times of interchange between WF and SO as presented in Fig. 11. The flow thresholds and the day of interchange between WF and SO are given in Table 4. Notice that the variation of the flow and the day index in the hydrograph is the same.

It is much interesting to note that the S–Q curves for various amplitudes in Fig. 10 show similarities with some types of salt intrusion curves (S-x, where x the longitudinal direction with x increasing upstream). In particular, the shape of the S–Q curves for the low tidal level scenarios resembles a lot the dome-shaped salt intrusion curves at least for low and medium flows. At the same time, the shape of the S–Q curves of the high tidal level scenarios seems to be very similar with that of recession-shaped salt intrusion curves. The shape of salt intrusion curves is determined by the van der Burgh coefficient K (Savenije 2005) which is small when tidal damping is low (e.g. microtidal) and large when tidal damping is high (e.g. macrotidal). Therefore, dome shape curves occur when K is large and recession-shaped ones when K is small (Savenije 2005). A correspondence seems to exist then between the changes of S-x curves with dispersion (as controlled by Van der Burgh) and the changes of S–Q with the amplitude (due to bathymetric effects).

Effects of the Inlet's Length on the Results

An important parameter to consider in the cases with tidal forcing is the effect of seasonal river discharge and the inlet's dimensions on tidal wave propagation. Figure 1b shows a sloping bed inside the inlet with the depth decreasing along a distance of 1 km upstream of the delta apex. The tide in sloping river beds propagates differently between high and low flow periods (Kastner et al. 2019). The tide gradually damps with its amplitude decreasing exponentially along the channel during both high and low flows but with a lower rate in the latter case (Ippen 1966; Friedrichs 2010) when the tidal influence is stronger (Kastner et al. 2019). The tidal influence at the short reach that connects the river with the sea can be significant even during high flows periods (Kastner et al. 2019). If the tide is reflected at the coast (inflow river boundary), a standing wave can be developed with its transport and elevation out of phase by 90° (Hoitink and Jay 2016). In nature, the standing wave can exist only at the point of reflection while the tide is allowed to propagate along the channel as if it were partially reflected without losing its energy to reflection (Hoitink and Jay 2016). In this idealized model though, there is a concern that the short reach may cut off the tidal prism, decreasing the tidal velocity and thus salinity intrusion. The contingency that the inlet's length may affect the results and conclusions of this paper has been investigated by doubling the model's size longitudinally and increasing the length of the inlet by 20 km while the bathymetry remains the same. Model settings are identical between the two cases (short and longer reach). The work was repeated and it was discovered that indeed the tidal velocity is higher in this case as expected. Figures and results from the simulations with the longer reach model (all available in chapter 3 of the 'Online Resource') indicate that despite the quantitative differences between the two cases the main conclusions of this paper are unaffected.

The higher tidal velocity increases the salinity but also causes a more symmetric distribution in consistency with what has been documented in 'Horizontal Salinity

Table 4 The value and index in the hydrograph of the maximum flow in each S–Q curve of the three bathymetry-controlled simulations in Fig. 10 and the flow magnitude at the time of interchange from WF to SO in Fig. 11. The time instant of interchange from WF to SO method coincides with the time instant of interchange from double to single exponential equation between salinity and river discharge

Tidal amplitude	No tide (0 m)	Nano-tide (0.02 m)	Microtide (0.15 m)
Flow threshold (m³/s)	120	133	87
Day index in the hydrograph	109	116	92
Day of interchange between WF and SO	109	116	92

Distribution and Flow Field Evolution with the Tidal Variation'. Consequently, even though the time period with freshwater in the delta becomes shorter for every simulation as a result of the increased salinity, the microtide case still exhibits the longer freshwater period supporting the argument that river-dominated systems could benefit from a small amplitude increase. In addition, the transition of the buoyant plume's vertical structure from surface to bottom-advected type as the amplitude increases can be observed in the long reach model as well.

Most importantly, the basic relationships presented in this paper remain unaffected. The salinity–river discharge relationship presents a single exponential correlation for the two maximum amplitude simulations (scenarios 4 and 5) and a double exponential one for the three bathymetry-controlled cases (scenarios 1, 2 and 3) in accordance to the short reach model results. Likewise, the salinity–stream order relationship is present when symmetric spatially salinity distributions are developed. Since the salinity distributions are more symmetric than before in the long reach model, the microtide scenario exhibits the salinity–stream order relationship in the entire simulation period in contrast to what is observed in the short reach model. However, the effects on this relationship from bathymetry are still detectable in the river-dominated systems.

This outcome supports further the argument in 'Salinity Model Setup' that in an idealized study the model testing should focus on the trends between variables and not their actual magnitudes.

Comparison with a Real Case Study

To strengthen and support the validity of the conclusions derived from the idealized model, a comparison is done with results from a similar work for a real case study. Bellafiore et al. (2021) implemented a numerical model to investigate the saltwater intrusion in the Po Delta under low river discharge conditions. In addition, they evaluated the response of the river delta to climate change by implementing a number of scenarios with different estimations for future sea level, air–sea fluxes and reduced discharges. Although they do not consider tidal variations in their model, their results for increased sea level and reduced discharges show much similarity with these of the present work where tidal amplitude increases and flow seasonality have been considered. One of their main considerations is that changes of river discharge are more influential to SWI than those of SLR. A look in the panels of Figs. 2 and 3 from the left to the right reveals much larger scale salinity changes from dry to wet seasons compared with these induced by TA changes. Moreover, they found that salt water intrusion in the main branches of the Po Delta is expected to extend by 80% for a scenario of relative sea level rise to 63 cm and a decrease of river discharge to 300–350 m3/s by 2100. A significant SWI

extension is also noticed inside the idealized delta channels for the maximum amplitudes in the panels of Fig. 4. In this case, only a small number of channels are filled with freshwater even during the maximum flow times while the FWA covers almost the entire delta in the low amplitude scenarios at the same times. The SWI extension becomes maximum during flood tide. A comparison of the 2 g/kg isohaline limits between the no tide and the macro-tide scenario shows an upstream displacement in the latter case by approximately 2 km in the longitudinal and 1.5 km in the lateral direction (Fig. 4c). However, an important finding of the present work is the positive effect that small increases of the TA can have against SWI because of the tide's contribution to mixing. This is much reflected at the number of days with freshwater in the delta for each simulation as presented in Fig. 9. Longer freshwater conditions were established in the delta in the microtide simulation compared to the no tide case. Bellafiore et al. (2021) measured the percentage of time with salinity higher than 2 g/kg in a 3-month simulation with reduced discharges to estimate the persistence of SWI in future SLR scenarios. In 'Relation Between Salinity and Delta's Bifurcation', the amount of time with salinity less than 2 g/kg has been measured instead when averaged between channels of equal order. It was found that channels of 1st- and 2nd-order that lie closer to the sea do not become fresh at all in the simulations with mesotide and macrotide conditions. Similar to this, Bellafiore et al. (2021) predicted a 100% SWI persistence for a 2081–2100 sea level scenario in the central node of the Po Delta where channels with close proximity to the sea meet. These channels could also be considered channels of 1st and/or 2nd order due to their position in the system and fewer number of bifurcations. Finally, Bellafiore et al. (2021) argue on the effect of morphology and depth changes from SLR to the SWI response to changes of forcing factors (e.g. tide). This agrees with our results as the bathymetry was found to have a strong influence on the salinity distribution and its correlations with river discharge and bifurcation order.

Conclusions

A 3D idealized delta model was built in Delft3D to investigate the combined impact of tides and varying river flow on the salinity in deltaic systems. The model was forced by seasonally varying freshwater flow from the river head and a tidal level prescribed at the offshore boundary. A symmetric beta flow distribution that is close to a Gaussian shape was implemented with very low and high flows allowing to detect different patterns developed at both dry and wet seasons. A series of five simulations with different amplitudes was carried out where both river-dominated and tidally influenced cases were considered.

Changes in the tidal amplitude in deltaic systems may have either positive or negative effects depending on their initial state. Increases of amplitude in river-dominated or low tidal systems were found to offer several advantages. The tide enhances the mixing in the delta and widens areas of brackish or freshwater. This flow enhancement is beneficial during the low flow periods because it helps to override bathymetric effects that produce asymmetric spatial salinity distribution leaving large areas with very high salinity. Tidal amplitude and river discharge increases lead progressively to more symmetric distributions. In addition, imposing medium tidal amplitudes extends the time the delta remains fresh during the wet season. Tide-induced mixing increases the freshwater volume in the delta compared to the river-dominated cases where the river discharge influence on the salinity weakens in the most distant from the delta apex areas that remain either partially mixed or stratified during the wet season. However, the freshwater is constrained in narrow areas around the inlet and its volume decreases significantly when the amplitude corresponds to meso- and macrotide regimes. This results in the delta containing freshwater for shorter time periods compared to the river-dominated and microtide cases. Tidal amplitude increases in such systems will deteriorate the conditions in terms of salinization. In such cases, an amplitude decrease would be favourable instead.

An offshore buoyant plume develops at flood tides with its vertical structure being determined by the tidal amplitude. Low amplitudes favour surface-advected and high-amplitude bottom-advected plumes. Surface-advected plumes may have several consequences on the water quality offshore of the delta counterbalancing the positive effects of tides inside the delta in low and medium amplitude regimes.

Finally, the role of bathymetry was found to be important because it affects the spatial salinity distribution. This has an impact on several salinity relations that were found to exist in a previous idealized study done for a case without tides. The salinity increases as the channels order decreases as long as its distribution remains symmetric and unaffected by bathymetry. In this case, the width function is suggested as an alternative where the salinity decreases as the width increases. The stream order method was successful at times of high and the width function at times of low flows. Asymmetric distributions do affect also the exponential correlation between radial salinity averages and river discharge. As long as the spatial salinity distribution is not symmetric, the two magnitudes are correlated by a double exponential equation that shows similarities with the solution of the 1D advection–diffusion equation in the presence of a wall boundary preventing the flow behind of it. Therefore, it is inferred that the methods are not affected by tidal forcing but can be sensitive to bathymetric differences.

References

Alber, M., and J.E. Sheldon. 1999. Use of a date-specific method to examine variability in the flushing times of Georgia estuaries. *Estuarine, Coastal and Shelf Science* 49 (4): 469–482. https://doi.org/10.1006/ecss.1999.0515.

Allison, L.E. 1964. Salinity in relation to irrigation', *Advances in Agronomy* 16(C): 139–180. https://doi.org/10.1016/S0065-2113(08)60023-1.

Andrews, S.W., E.S. Gross, and P.H. Hutton. 2017. Modeling salt intrusion in the San Francisco Estuary prior to anthropogenic influence. *Continental Shelf Research. Elsevier Ltd* 146 (May): 58–81. https://doi.org/10.1016/j.csr.2017.07.010.

Atkinson, J.F. 1993. Detachment of buoyant surface jets discharged on slope. *Journal of Hydraulic Engineering* 119 (8): 878–894. https://doi.org/10.1061/(asce)0733-9429(1993)119:8(878).

Banas, N.S., B.M. Hickey, P. MacCready, and J.A. Newton. 2004. Dynamics of Willapa Bay, Washington: A highly unsteady, partially mixed estuary. *Journal of Physical Oceanography* 34 (11): 2413–2427. https://doi.org/10.1175/JPO2637.1.

Bellafiore, D., C. Ferrarin, F. Maicu, G. Manfe, G. Lorenzetti, G. Umgiesser, L. Zaggia, and A. Valle-Levinson. 2021. Saltwater intrusion in a Mediterranean delta under a changing climate. *Journal of Geophysical Research: Oceans*. https://doi.org/10.1029/2020JC016437.

Bhuiyan, M.J.A.N., and D. Dutta. 2012. 'Assessing impacts of sea level rise on river salinity in the Gorai river network, Bangladesh', Estuarine. *Coastal and Shelf Science. Elsevier Ltd* 96 (1): 219–227. https://doi.org/10.1016/j.ecss.2011.11.005.

Bianchi, T.S. 2016. Deltas and humans:A long relationship now threatened by global change. Oxford University Press.

Birkinshaw, S.J., S.B. Guerreiro, A. Nicholson, Q. Liang, P. Quinn, L. Zhang, B. He, J. Yin, and H.J. Fowler. 2017. Climate change impacts on Yangtze River discharge at the Three Gorges Dam. *Hydrology and Earth System Sciences* 21 (4): 1911–1927. https://doi.org/10.5194/hess-21-1911-2017.

Botter, G., and A. Rinaldo. 2003. Scale effect on geomorphologic and kinematic dispersion. *Water Resources Research* 39 (10): 1–10. https://doi.org/10.1029/2003WR002154.

Bowen, M.M., and W.R. Geyer. 2003. Salt transport and the time-dependent salt balance of a partially stratified estuary. *Journal of*

Geophysical Research 108 (C5): 1–15. https://doi.org/10.1029/2001jc001231.

Bricheno, L.M., and J. Wolf. 2018. 'Modeling Tidal River Salinity in Coastal Bangladesh', chapter 17 in Ecosystem services for Well-Being Deltas,Integrated Analysis for Policy Analysis. https://doi.org/10.1007/978-3-319-71093-8

Bricheno, L.M., J. Wolf, and S. Islam. 2016. 'Tidal intrusion within a mega delta: An unstructured grid modelling approach', *Estuarine, Coastal and Shelf Science*. The Authors 182: 12–26. https://doi.org/10.1016/j.ecss.2016.09.014.

Bricheno, L.M., J. Wolf, and Y. Sun. 2021. 'Saline intrusion in the Ganges-Brahmaputra-Meghna megadelta', Estuarine. *Coastal and Shelf Science. Elsevier Ltd* 252: 107246. https://doi.org/10.1016/j.ecss.2021.107246.

Burpee, A.P., R.L. Slingerland, D.A. Edmonds, D. Parsons, J. Best, J. Cederberg, A. McGuffin, R. Caldwell, A. Nijhuis, and J. Royce. 2015. Grain-size controls on the morphology and internal geometry of river-dominated deltas. *Journal of Sedimentary Research* 85 (6): 699–714. https://doi.org/10.2110/jsr.2015.39.

Caldwell, R., and D.A. Edmonds. 2014. The effects of sediment properties on deltaic processes and morphologies: A numerical modeling study. *Journal of Geophysical Research* 961–982. https://doi.org/10.1002/2013JF002871.Received.

Carless, S.J., J.A.M. Greena, H.E. Pelling, and S.B. Wilmes. 2016. 'Effects of future sea-level rise on tidal processes on the Patagonian Shelf', *Journal of Marine Systems*. The Authors 163: 113–124. https://doi.org/10.1016/j.jmarsys.2016.07.007.

Chant, R.J. 2012. Interactions between estuaries and coasts: river plumes - their formation, transport, and dispersal, treatise on estuarine and coastal science. Elsevier Inc. https://doi.org/10.1016/B978-0-12-374711-2.00209-6.

Chao, S.Y. 1988. River-forced estuarine plumes. *J. Phys. Oceanogr*, 72–88. https://doi.org/10.1175/1520-0485(1988)018<0072:rfep>2.0.co;2.

Chao, S.Y. 1990. Tidal modulation of estuarine plumes. *Journal of Physical Oceanography* 1115–1123. https://doi.org/10.1175/1520-0485(1990)020<1115:TMOEP>2.0.CO;2.

Chao, S.Y., and W.C. Boicourt. 1986. Onset of estuarine plumes. *J. Phys. Oceanogr* 2137–2149. https://doi.org/10.1016/0198-0254(87)90056-2.

Chapman, D.C., and S.J. Lentz. 1994. Trapping of a coastal density front by the bottom boundary layer. *Journal of Physical Oceanography* 1464–1479. https://doi.org/10.1175/1520-0485(1994)024<1464:TOACDF>2.0.CO;2.

Chen, F., and D.G. MacDonald. 2006. Role of mixing in the structure and evolution of a buoyant discharge plume. *Journal of Geophysical Research: Oceans* 111 (11): 1–13. https://doi.org/10.1029/2006JC003563.

Chen, X., Y. Zong, E. Zhang, J. Xu, and S. Li. 2001. Human impacts on the Changjiang (Yangtze) River basin, China, with special reference to the impacts on the dry season water discharges into the sea. *Geomorphology* 41 (2): 111–123. https://doi.org/10.1016/S0169-555X(01)00109-X.

Chen, X.J. 2004. Modeling hydrodynamics and salt transport in the Alafia River estuary, Florida during May 1999-December 2001. *Estuarine, Coastal and Shelf Science* 61 (3): 477–490. https://doi.org/10.1016/j.ecss.2004.06.012.

Chua, V.P., and M. Xu. 2014. Impacts of sea-level rise on estuarine circulation: an idealized estuary and San Francisco Bay. *Journal of Marine Systems*. Elsevier B.V. 139: 58–67. https://doi.org/10.1016/j.jmarsys.2014.05.012.

Chunikhina, E.V. 2018. Entropy rates for Horton self-similar trees. *School of EECS, Oregon State University, Corvallis, OR* 977330: 1–20.

Cole, K.L., and R.D. Hetland. 2016. The effects of rotation and river discharge on net mixing in small-mouth Kelvin number plumes. *Journal of Physical Oceanography* 46 (5): 1421–1436. https://doi.org/10.1175/JPO-D-13-0271.1.

Collischonn, W., A. Fleischmann, R.C.D. Paiva, and A. Mejia. 2017. Hydraulic causes for basin hydrograph skewness. *Water Resources Research* 53: 10603–10618. https://doi.org/10.1002/2017WR021543.

Csanady, G.T. 1984. Circulation induced by river inflow in well mixed water over a sloping continental shelf. *J. PHYS. OCEANOGR.* 14(11, Nov. 1984): 1703–1711. https://doi.org/10.1175/1520-0485(1984)0142.0.CO;2.

Dai, Z., A. Chu, M. Stive, X. Zhang, and H. Yan. 2011. Unusual salinity conditions in the Yangtze Estuary in 2006: Impacts of an extreme drought or of the three gorges dam? *Ambio* 40 (5): 496–505. https://doi.org/10.1007/s13280-011-0148-2.

Dasgupta, S., F.A. Kamal, Z.H. Khan, S. Choudhury, and A. Nishat. 2015. River salinity and climate change: evidence from coastal Bangladesh. *World Scientific Reference on Asia and the World Economy*, pp. 205–242. https://doi.org/10.1142/9789814578622_0031.

Day, J.W., J. Barras, E. Clairain, J. Johnston, D. Justic, G.P. Kemp, J.Y. Ko, R. Lane, W.J. Mitsch, G. Steyer, P. Templet, and A. Yanez-Arancibia. 2005. Implications of global climatic change and energy cost and availability for the restoration of the Mississippi delta. *Ecological Engineering* 24(4 SPEC. ISS.): 253–265. https://doi.org/10.1016/j.ecoleng.2004.11.015.

de Nijs, M.A.J., and J.D. Pietrzak. 2012. 'Saltwater intrusion and ETM dynamics in a tidally-energetic stratified estuary', *Ocean Modelling. Elsevier Ltd* 49–50: 60–85. https://doi.org/10.1016/j.ocemod.2012.03.004.

de Vos, A. 1990. *Crop salt tolerance under controlled field conditions in The Netherlands, based on trials conducted at Salt Farm Texel.* Manuals and Reports on Engineering Practice: American Society of Civil Engineers.

Deltares (2013) *Delft3D-FLOW user manual*.

Du, J., J. Shen, Y.J. Zhang, F. Ye, Z. Liu, Z. Wang, Y.P. Wang, X. Yu, M. Sisson, and H.V. Wang. 2018. Tidal response to sea-level rise in different types of estuaries: The importance of length, bathymetry, and geometry. *Geophysical Research Letters* 45 (1): 227–235. https://doi.org/10.1002/2017GL075963.

Dyer, K.R. 1973. Estuaries: A Physical Introduction. John Wiley and sons, London, UK.

Edmonds, D.A., and R.L. Slingerland. 2010. Significant effect of sediment cohesion on deltamorphology. *Nature Geoscience. Nature Publishing Group* 3 (2): 105–109. https://doi.org/10.1038/ngeo730.

Elhakeem, A., and W. Elshorbagy. 2013. Evaluation of the long-term variability of seawater salinity and temperature in response to natural and anthropogenic stressors in the Arabian Gulf. *Marine Pollution Bulletin. Elsevier Ltd* 76 (1–2): 355–359. https://doi.org/10.1016/j.marpolbul.2013.08.036.

Ericson, J., C. Vorosmarty, S. Dingman, L. Ward, and M. Meybeck. 2006. Effective sea-level rise and deltas: Causes of change and human dimension implications. *Global and Planetary Change* 50 (1–2): 63-82 S0921818105001827. https://doi.org/10.1016/j.gloplacha.2005.07.004.

Eslami, S., P. Hoekstra, N.N. Trung, S.A. Kantoush, D. Van Binh, D.D. Dung, and Tho tran Quang, van der Vegt M. 2019. Tidal amplification and salt intrusion in the Mekong Delta driven by anthropogenic sediment starvation. *Scientific Reports* 9 (1): 1–10. https://doi.org/10.1038/s41598-019-55018-9.

Fagherazzi, S., D.A. Edmonds, W. Nardin, N. Leonardi, A. Canestrelli, F. Falcini, D.J. Jerolmack, G. Mariotti, J.C. Rowland, and R.L. Slingerland. 2015. Dynamics of river mouth deposits. *Reviewes of Geophysics'* 53: 642–672. https://doi.org/10.1002/2014RG000451.

Fischer, H.B., E.J. List, and R.C.Y. Koch, J. Imberger, N.H. Brooks. 1979. 'Mixing in Inland and Coastal Waters', chapter 2. Academic Press, New York.

Friedrichs, C.T. 2010. Barotropic tides in channelized estuaries. In *Contemporary Issues in Estuarine Physics*, ed. A. Valle-Levinson, 27–61. Cambridge: Cambridge University Press.

Frihy, O.E. 2003. The nile delta-Alexandria coast: Vulnerability to sea-level rise, consequences and adaptation. *Mitigation and Adaptation Strategies for Global Change* 8 (2): 115–138. https://doi.org/10.1023/A:1026015824714.

Garvine, R.W. 1999. Penetration of buoyant coastal discharge onto the continental shelf: A numerical model experiment. *Journal of Physical Oceanography* 29(8 PART 2): 1892–1909. https://doi.org/10.1175/1520-0485(1999)029<1892:pobcdo>2.0.co;2.

Geyer, W.R., and P. MacCready. 2014. The estuarine circulation. *Annual Review of Fluid Mechanics* 46: 175–197. https://doi.org/10.1146/annurev-fluid-010313-141302.

Gleyzer, A., M. Denisyuk, A. Rimmer, and Y. Salingar. 2004. A fast recursive GIS algorithm for computing Strahler stream order in braided and non-braided networks. *Journal of the American Water Resources Association* 2004: 937–946.

Gong, W., and J. Shen. 2011. The response of salt intrusion to changes in river discharge and tidal mixing during the dry season in the Modaomen Estuary, China. *Continental Shelf Research. Elsevier* 31 (7–8): 769–788. https://doi.org/10.1016/j.csr.2011.01.011.

Goodbred, S.L. Jr, and Y. Saito. 2012. Tide-dominated deltas, chapter 7 in *Principles of tidal sedimentology.* edited by Davis, R.A.Jr and Dalrymple, R.W., https://doi.org/10.1007/978-94-007-0123-6_7, Springer Science+Business Media B.V. 2012

Gornitz, V. 1991. Global coastal hazards from future sea level rise. *Palaeogeography, Palaeoclimatology, Palaeoecology* 89 (4): 379–398. https://doi.org/10.1016/0031-0182(91)90173-O.

Green, J.A.M. 2010. Ocean tides and resonance. *Ocean Dynamics* 60 (5): 1243–1253. https://doi.org/10.1007/s10236-010-0331-1.

Guo, X., and A. Valle-Levinson. 2007. Tidal effects on estuarine circulation and outflow plume in the Chesapeake Bay. *Continental Shelf Research* 27 (1): 20–42. https://doi.org/10.1016/j.csr.2006.08.009.

Gupta, V.K., and O.J. Mesa. 1988. Runoff generation and hydrologic response via channel network geomorphology - recent progress and open problems. *Journal of Hydrology* 102 (1–4): 3–28. https://doi.org/10.1016/0022-1694(88)90089-3.

Haigh, I.D., M.D. Pickering, J.A. Mattias Green, B.K. Arbic, A. Arns, S. Dangendorf, D.F. Hill, K. Horsburgh, T. Howard, D. Idier, D.A. Jay, L. Janicke, S.B. Lee, M. Muller, M. Schindelegger, S.A. Talke, S.B. Wilmes, and P.L. Woodworth. 2020. The tides they are A-Changin': A comprehensive review of past and future nonastronomical changes in tides, their driving mechanisms, and future implications. *Reviews of Geophysics* 58 (1): 1–39. https://doi.org/10.1029/2018RG000636.

Hansen, D.V., and M. Jr. Rattray. 1965.'Gravitational Circulation in Straits & Estuaries', *Journal of Marine Research*, 23 (2): 104-122.

Hoitink, A.J.F., and D.A. Jay 2016. Tidal river dynamics: implications for deltas. *Reviews of Geophysics.* 54: 240–272. https://doi.org/10.1002/2015RG000507.

Holleman, R.C., and M.T. Stacey. 2014. Coupling of sea level rise, tidal amplification, and inundation. *Journal of Physical Oceanography* 44 (5): 1439–1455. https://doi.org/10.1175/JPO-D-13-0214.1.

Holm, J., and C.E. Sasser. 2001. Differential salinity response between two Mississippi River subdeltas: Implications for changes in plant composition. *Estuaries* 24 (1): 78–89. https://doi.org/10.2307/1352815.

Hong, B., Z. Liua, J. Shen, H. Wu, W. Gong, H. Xu, and D. Wang. 2020. Potential physical impacts of sea-level rise on the Pearl River Estuary, China. *Journal of Marine Systems. Elsevier* 201: 103245. https://doi.org/10.1016/j.jmarsys.2019.103245.

Hong, B., and J. Shen. 2012. 'Responses of estuarine salinity and transport processes to potential future sea-level rise in the Chesapeake Bay', *Estuarine, Coastal and Shelf Science. Elsevier Ltd* 104–105: 33–45. https://doi.org/10.1016/j.ecss.2012.03.014.

Hori, K., Y. Saito, Q. Zhao, and P. Wang. 2002. 'Architecture and evolution of the tide-dominated Changjiang (Yangtze) River delta. *China', Sedimentary Geology* 146: 249–264.

Hori K., and Y. Saito. 2007. Classification, architecture and evolution of large-river deltas. Large Rivers: Geomorphology and Management, Chapter 6.

Horton, R.E. 1945. 'Erosional development of streams and their drainage basins. *Hydrophysical Approach to Quantitative Morphology', Bulletin of the Geological Society of America '* 56 (March): 275–370.

Hu, K., P. Ding, Z. Wang, and S. Yang. 2009. A 2D/3D hydrodynamic and sediment transport model for the Yangtze Estuary, China. *Journal of Marine Systems.* Elsevier B.V., 77(1–2): 114–136. https://doi.org/10.1016/j.jmarsys.2008.11.014.

Hutton, P.H., J.S. Rath, L. Chen, M.J. Ungs, S.B. Roy, and A.M. ASCE. 2016. Nine decades of salinity observations in the San Francisco bay and delta: Modeling and trend evaluations. *Journal of Water Resources Planning and Management* 142 (3): 1–11. https://doi.org/10.1061/(ASCE)WR.1943-5452.0000617.

Idier, D., F. Paris, G. Le Cozannet, F. Boulahya, and F. Dumas. 2017. Sea-level rise impacts on the tides of the European Shelf. *Continental Shelf Research. Elsevier Ltd* 137 (January): 56–71. https://doi.org/10.1016/j.csr.2017.01.007.

Ippen, A.T. 1966. *Estuary and coastline hydrodynamics*. McGraw-Hill.

Isobe, A. 2005. Ballooning of river-plume bulge and its stabilization by tidal currents. *Journal of Physical Oceanography* 35 (12): 2337–2351. https://doi.org/10.1175/JPO2837.1.

Jassby, A.D., W.J. Kimmerer, S.G. Monismith, C. Armor, J.E. Cloern, T.M. Powell, J.R. Schubel, and T.J. Vendlinski. 1995. Isohaline position as a habitat indicator for estuarine populations. *Ecological Applications* 5 (1): 272–289. https://doi.org/10.2307/1942069.

Jay, D.A. 1991. Green's law revisited: Tidal long-wave propagation in channels with strong topography. *Journal of Geophysical Research* 96 (C11): 20585. https://doi.org/10.1029/91jc01633.

Jay, D.A., and J.D. Musiak. 1994. Particle trapping in estuarine tidal flows. *Journal of Geophysical Research* 99(C10). https://doi.org/10.1029/94jc00971.

Jiang, L., T. Gerkema, D. Idier, A.B.A. Slangen, and K. Soetaert. 2020. Effects of sea-level rise on tides and sediment dynamics in a Dutch tidal bay. *Ocean Science* 16 (2): 307–321. https://doi.org/10.5194/os-16-307-2020.

Kaplan, D., R.M. Carpena, Y. Wan, M. Hedgepeth, F. Zheng, R. Roberts, and R. Rossmanith. 2010. Linking River, floodplain, and vadose zone hydrology to improve restoration of a coastal river affected by saltwater intrusion. *Journal of Environmental Quality* 39 (5): 1570–1584. https://doi.org/10.2134/jeq2009.0375.

Kastner, K., A.J.F. Hoitink, P.J.J.F. Torfs, E. Deleersnijder, and N.S. Ningsih. 2019. Propagation of tides along a river with a sloping bed. *Journal ofFluid Mechanics* 872: 39–73.

Kirkby, M.J. 1976. Tests of the random network model, and its application to basin hydrology. *Earth Surface Processes* 1 (3): 197–212. https://doi.org/10.1002/esp.3290010302.

Kourafalou, V.H., L.Y. Oey, J.D. Wang, and T.N. Lee. 1996. The fate of river discharge on the continental shelf 1. Modeling the river plume and the inner shelf coastal current. *Journal of Geophysical Research c: Oceans* 101 (C2): 3415–3434. https://doi.org/10.1029/95JC03024.

Lai, X., Q. Huang, Y. Zhang, and J. Jiang. 2014. Impact of lake inflow and the Yangtze River flow alterations on water levels in Poyang Lake, China. *Lake and Reservoir Management* 30 (4): 321–330. https://doi.org/10.1080/10402381.2014.928390.

Lamb, M.P., et al. 2012. Backwater and river plume controls on scour upstream of river mouths: Implications for fluvio-deltaic morphodynamics. *Journal of Geophysical Research: Earth Surface* 117 (1): 1–16. https://doi.org/10.1029/2011JF002079.

Lee, J., and A. Valle-Levinson. 2013. Bathymetric effects on estuarine plume dynamics. *Journal of Geophysical Research: Oceans* 118 (4): 1969–1981. https://doi.org/10.1002/jgrc.20119.

Lerczak, J.A., W.R. Geyer, and R.J. Chant. 2006. Mechanisms driving the time-dependent salt flux in a partially stratified estuary. *Journal of Physical Oceanography* 36 (12): 2296–2311. https://doi.org/10.1175/JPO2959.1.

Liu, Y., H. Chen, J. Wang, S. Yang, and A. Chen. 2020. Numerical simulation for the effects of waves and grain size on deltaic processes and morphologies. *Open Geoscience* 12 (1): 1286–1301. https://doi.org/10.1515/geo-2020-0196.

Liu, B., S. Peng, Liao Y. Yeying, and H. Wang. 2019. The characteristics and causes of increasingly severe saltwater intrusion in Pearl River Estuary, Estuarine. *Coastal and Shelf Science. Elsevier* 220: 54–63. https://doi.org/10.1016/j.ecss.2019.02.041.

Liu, W.C., Wei-Bo Chen, R.T. Cheng, Ming-Hsi. Hsu, and A.Y. Kuo. 2007. Modeling the influence of river discharge on salt intrusion and residual circulation in Danshuei River estuary, Taiwan. *Continental Shelf Research* 27 (7): 900–921. https://doi.org/10.1016/j.csr.2006.12.005.

MacCready, P. 2007. Estuarine adjustment. *Journal of Physical Oceanography* 37 (8): 2133–2145. https://doi.org/10.1175/JPO3082.1.

MacCready, P., and W.R. Geyer. 2010. Advances in estuarine physics. *Annual Review of Marine Science* 2 (1): 35–58. https://doi.org/10.1146/annurev-marine-120308-081015.

Maccready, P., W.R. Geyer, and H. Burchard. 2018. Estuarine exchange flow is related to mixing through the salinity variance budget. *Journal of Physical Oceanography* 48 (6): 1375–1384. https://doi.org/10.1175/JPO-D-17-0266.1.

Maicu, F., F. De Pascalis, C. Ferrarin, and G. Umgiesser. 2018. Hydrodynamics of the Po River-Delta-Sea System. *Journal of Geophysical Research: Oceans*, 123(9): 6349–6372. https://doi.org/10.1029/2017JC013601.

Martyr-Koller, R.C., H.W.J. Kernkamp, A. van Dam, M. van der Wegen, L.V. Lucas, N. Knowles, B. Jaffe, and T.A. Fregoso. 2017. Application of an unstructured 3D finite volume numerical model to flows and salinity dynamics in the San Francisco Bay-Delta. *Estuarine, Coastal and Shelf Science* 192: 86–107.

Matsoukis, C., L.O. Amoudry, L. Bricheno, and N. Leonardi. 2021. Investigation of spatial and temporal salinity distribution in a river dominated delta through idealized numerical modelling. *Estuaries and Coasts*.

Monismith, S.G., W. Kimmerer, J.R. Burau, and M.T. Stacey. 2002. Structure and flow-induced variability of the subtidal salinity field in northern San Francisco Bay. *Journal of Physical Oceanography* 32 (11): 3003–3019.

Montanari, A. 2012. Hydrology of the Po River: Looking for changing patterns in river discharge. *Hydrology and Earth System Sciences* 16 (10): 3739–3747. https://doi.org/10.5194/hess-16-3739-2012.

Moussa, R. 2009. Definition of new equivalent indices of Horton-Strahler ratios for the derivation of the geomorphological instantaneous unit hydrograph. *Water Resources Research* 45 (9): 1–24. https://doi.org/10.1029/2008WR007330.

Murray, A.B. 2003. Contrasting the goals, strategies and predictions associated with simplified numerical models and detailed simulations. *Geophysical Monograph Series, Prediciton in Geomorphology.* https://doi.org/10.1029/135GM11.

Murray, A.B. 2002. Seeking explanation affects numerical modeling strategies. *Eos* 83 (38): 418–419. https://doi.org/10.1029/2002EO000304.

Narayanan, C., and R.W. Garvine. 2002. Large scale buoyancy driven circulation on the continental shelf. *Dynamics of Atmospheres and Oceans* 36 (1–3): 125–152. https://doi.org/10.1016/S0377-0265(02)00028-3.

Nguyen, A.D., and H.H.G. Savenije. 2006. Salt-intrusion in multi-channel estuaries: a case study in the Mekong Delta, Vietnam. *Hydrology and Earth System Sciences*, 10 (5): 743-754.

Nguyen, A.D., H.H.G. Savenije, D.N. Pham, and D.T. Thang Tang. 2008. Using salt intrusion measurements to determine the freshwater discharge distribution over the branches of a multi-channel estuary: The Mekong Delta case. *Estuarine, Coastal and Shelf Science* 77 (3): 433–445. https://doi.org/10.1016/j.ecss.2007.10.010.

Nhan, Nguyen Huu. 2016. 'Tidal regime deformation by sea level rise along the coast of the Mekong Delta', *Estuarine, Coastal and Shelf Science. Elsevier Ltd* 183: 382–391. https://doi.org/10.1016/j.ecss.2016.07.004.

Nicholls, R.J., C.W. Hutton, W.N. Adger, S.C. Hanson, M.M. Rahman, and M. Salehin. 2018. Ecosystem Services for Well-Being in Deltas: Integrated Assessment for Policy Analysis. https://doi.org/10.1007/978-3-319-71093-8.

O'Donnell, J. 1990. The formation and fate of a river plume: a numerical model. *J. Physical Oceanography* 551–569. https://doi.org/10.1175/1520-0485(1990)020<0551:TFAFOA>2.0.CO;2.

Oye, Lie-yaw. 1992. Subtidal variability of estuarine outflow, plume and coastal current: A model study. *Journal of Physical Oceanography* 23 (2): 164–171.

Pelling, H.E., K. Uehara, and J.A.M. Green. 2013. The impact of rapid coastline changes and sea level rise on the tides in the Bohai Sea, China. *Journal of Geophysical Research: Oceans* 118 (7): 3462–3472. https://doi.org/10.1002/jgrc.20258.

Pickering, M.D., K.J. Horsburgh, J.R. Blundell, J.J.M. Hirschi, R. Nicholls, and M. Verlaan. 2017. 'The impact of future sea-level rise on the global tides.' *Continental Shelf Research. Elsevier Ltd* 142: 50–68. https://doi.org/10.1016/j.csr.2017.02.004.

Polonskii, V.F., and T.Y. Solodovnikova. 2009. Estimation of transformation of flood runoff hydrographs and water stages in the Lower Volga and its delta. *Russian Meteorology and Hydrology* 34 (9): 618–627. https://doi.org/10.3103/S1068373909090076.

Prandle, D. 2004. Saline intrusion in partially mixed estuaries. *Estuarine, Coastal and Shelf Science* 59 (3): 385–397. https://doi.org/10.1016/j.ecss.2003.10.001.

Pritchard,. 1956. The dynamic structure of a coastal plain estuary. *Journal of Marine Research* 15: 33–42.

Qiu, C., and J. Zhu. 2015. Assessing the influence of sea level rise on salt transport processes and estuarine circulation in the Changjiang River Estuary. *Journal of Coastal Research* 31 (3): 661–670. https://doi.org/10.2112/JCOASTRES-D-13-00138.1.

Rahman, M.M. 2015. The effect of rainfall, temperature and humidity on saline in the southern area of Bangladesh. *Foreign Affairs* 1689–1699. https://doi.org/10.1017/CBO9781107415324.004.

Rahman, M.M., G. Penny, M.S. Mondal, M.H. Zaman, A. Kryston, M. Salehin, Q. Nahar, M.S. Islam, D. Bolsterb, J.L. Tank, and M.F. Müller. 2019. Salinization in large river deltas: drivers, impacts and socio-hydrological feedbacks. *Water Security*. Elsevier, 6(October 2018): 100024. https://doi.org/10.1016/j.wasec.2019.100024.

Ralston, D.K., W.R. Geyer, and J.A. Lerczak. 2010. Structure, variability, and salt flux in a strongly forced salt wedge estuary. *Journal of Geophysical Research: Oceans* 115 (6): 1–21. https://doi.org/10.1029/2009JC005806.

Reis, A.H. 2006. Constructal view of scaling laws of river basins. *Geomorphology* 78 (3–4): 201–206. https://doi.org/10.1016/j.geomorph.2006.01.015.

Rinaldo, A., G.K. Vogel, R. Rigon, and I. Rodriguez-Iturbe. 1995. Can one gauge the shape of a basin? *Water Resources Research* 31 (4): 1119–1127. https://doi.org/10.1029/94WR03290.

Rinaldo, A., A. Marani, and R. Rigon. 1991. Geomorphological dispersion. *Water Resources Research* 27 (4): 513–525. https://doi.org/10.1029/90WR02501.

Sarwar, M.G.M. 2005. Impacts of sea level rise on the coastal zone of Bangladesh. *Response* 45.

Savenije, H.H.G. 2005. Salinity and tides in alluvial estuaries. *Delft University of Technology*.

Schiller, R.V., V.H. Kourafalou, P. Hogan, and N.D. Walker. 2011. The dynamics of the Mississippi River plume: Impact of topography, wind and offshore forcing on the fate of plume waters. *Journal of Geophysical Research: Oceans* 116 (6): 1–22. https://doi.org/10.1029/2010JC006883.

Schubel, J.R. 1992. *San Francisco Estuary Project*. https://doi.org/10.4135/9781452231389.n24.

Sherin, V.R., F. Durand, F. Papa, A.K.M. Saiful Islam, V.V. Gopalakrishna, M. Khaki, and V. Suneel. 2020. Recent salinity intrusion in the Bengal delta: Observations and possible causes. *Continental Shelf Research. Elsevier Ltd* 202 (January): 104142. https://doi.org/10.1016/j.csr.2020.104142.

Simpson, J.H., J. Brown, J. Matthews, and G. Allen. 1990. Tidal straining, density currents, and stirring in the control of estuarine stratification. *Estuaries* 13 (2): 125–132. https://doi.org/10.2307/1351581.

Smart, J.S. 1968. Statistical properties of stream lengths. *Water Resources Research* 4 (5): 1001–1014. https://doi.org/10.1029/WR004i005p01001.

Smedema, L.K., and K. Shiati. 2002. Irrigation and salinity: A perspective review of the salinity hazards of irrigation development in the arid zone. *Irrigation and Drainage Systems* 16 (2): 161–174. https://doi.org/10.1023/A:1016008417327.

Snell, J.D., and M. Sivapalan. 1994. On geomorphological dispersion in natural catchments and the unit hydrograph. *Water Resources Research* 30 (7): 2311–2323.

Stacey, M.T., and D.K. Ralston. 2005. The scaling and structure of the estuarine bottom boundary layer. *Journal of Physical Oceanography* 35 (1): 55–71. https://doi.org/10.1175/JPO-2672.1.

Stelling, G.S., and J.J. Leendertse. 1992. Approximation of convective processes by Cyclic AOI methods. In M. L. Spaulding, K. Bedford and A. Blumberg, eds., *Estuarine and coastal modeling*, Proceedings 2nd Conference on Estuarine and Coastal Modelling, ASCE, 771–782.

Strahler, A.N. 1952. Hypsometric (area-altitude) analysis of erosional topology. *Geological Society of America Bulletin* 63 (11): 1117–1142.

Turrell, W.R., J. Brown, and J.H. Simpson. 1996. Salt intrusion and secondary flow in a shallow, well-mixed estuary. *Estuarine, Coastal and Shelf Science* 42 (2): 153–169. https://doi.org/10.1006/ecss.1996.0012.

Uncles, R.J., and J.A. Stephens. 1996. Salt intrusion in the Tweed Estuary. *Estuarine, Coastal and Shelf Science* 43 (3): 271–293. https://doi.org/10.1006/ecss.1996.0070.

Visser, J.M., J.W. Day, L.L. Battaglia, G.P. Shaffer, and M.W. Hester. 2012. Mississippi river delta wetlands. *Wetland Habitats of North America: Ecology and Conservation Concerns* 63–74. https://doi.org/10.1525/9780520951419-007.

Wei, X., G.P. Schramkowski, and H.M. Schuttelaars. 2016. Salt dynamics in well-mixed estuaries: Importance of advection by tides. *Journal of Physical Oceanography* 46 (5): 1457–1475. https://doi.org/10.1175/JPO-D-15-0045.1.

Weisberg, M. 2007. Three kinds of idealization. *Journal of Philosophy* 104 (12): 639–659. https://doi.org/10.5840/jphil20071041240.

White, E.D., E. Meselhe, D. Reed, A. Renfro, N.P. Snider, and Y. Wang. 2019. Mitigating the effects of sea-level rise on estuaries of the Mississippi Delta Plain using river diversions. *Water (Switzerland)* 11(10). https://doi.org/10.3390/w11102028.

White, E., and D. Kaplan, 2017. Restore or retreat? saltwater intrusion and water management in coastal wetlands. *Ecosystem Health and Sustainability* 3(1). https://doi.org/10.1002/ehs2.1258.

Wright, D.G. 1989. On the alongshelf evolution of an idealized density front. *Journal of Physical Oceanography* 19 (4): 532–541. https://doi.org/10.1175/1520-0485(1989)019%3c0532:otaeoa%3e2.0.co;2.

Yamamoto, K.E.N. 2017. Central limit theorem for the Horton - Strahler bifurcation ratio of general branch order. 1124(March 2017): 1111–1124. https://doi.org/10.1017/jpr.2017.55.

Yang, Y., T.A. Endreny, and D.J. Nowak. 2015. Simulating double-peak hydrographs from single storms over mixed-use watersheds. *Journal of Hydrologic Engineering* 20 (11): 1–5. https://doi.org/10.1061/(ASCE)HE.1943-5584.0001225.

Yankovsky, A.E., and D.C. Chapman. 1997. A simple theory for the fate of buoyant coastal discharges. *Journal of Physical Oceanography* 27 (7): 1386–1401. https://doi.org/10.1175/1520-0485(1997)027%3c1386:ASTFTF%3e2.0.CO;2.

Yue, S., T.B.M.J. Ouarda, B. Bobe, P. Legendre, and P. Bruneau. 2002. Approach for describing statistical properties of flood hydrograph. *Journal of Hydrologic Engineering* 7 (2): 147–153. https://doi.org/10.1061/(ASCE)1084-0699(2002)7:2(147).

Zhang, E., H.H.G. Savenije, H. Wu, Y. Kong, and J. Zhu. 2011. 'Analytical solution for salt intrusion in the Yangtze Estuary, China', Estuarine. *Coastal and Shelf Science. Elsevier Ltd* 91 (4): 492–501. https://doi.org/10.1016/j.ecss.2010.11.008.

Zhang, W., X. Ruan, J. Zheng, Y. Zhu, and H. Wu. 2010. Long-term change in tidal dynamics and its cause in the Pearl River Delta, China. *Geomorphology*. Elsevier B.V., 120(3–4): 209–223. https://doi.org/10.1016/j.geomorph.2010.03.031.

Zhong, L., M. Li, and M.G.G. Foreman. 2008. Resonance and sea level variability in Chesapeake Bay. *Continental Shelf Research* 28 (18): 2565–2573. https://doi.org/10.1016/j.csr.2008.07.007.